The Astrophysical Journal Supplement Series, 213:20 (28pp), 2014 August doi:10.1088/0067-0049/213/2/20

IBEX: THE FIRST FIVE YEARS (2009–2013)

D. J. McComas[1,2], F. Allegrini[1,2], M. Bzowski[3], M. A. Dayeh[1], R. DeMajistre[4], H. O. Funsten[5], S. A. Fuselier[1,2], M. Gruntman[6], P. H. Janzen[7], M. A. Kubiak[3], H. Kucharek[8], E. Möbius[8], D. B. Reisenfeld[7], N. A. Schwadron[1,8], J. M. Sokół[3], and M. Tokumaru[9]

[1] Southwest Research Institute, P.O. Drawer 28510, San Antonio, TX 78228, USA; dmccomas@swri.org
[2] University of Texas at San Antonio, San Antonio, TX 78249, USA
[3] Space Research Centre of the Polish Academy of Sciences, Bartycka 18A, 00-716 Warsaw, Poland
[4] Applied Physics Laboratory, Johns Hopkins University, 11100 Johns Hopkins Road, Laurel, MD 20723, USA
[5] Los Alamos National Laboratory, Intelligence and Space Research Division, P.O. Box 1663, Los Alamos, NM 87545, USA
[6] Department of Astronautical Engineering, Viterbi School of Engineering, University of Southern California, Los Angeles, CA 90089-1192, USA
[7] University of Montana, 32 Campus Drive, Missoula, MT 59812, USA
[8] Space Science Center, University of New Hampshire, Morse Hall Room 407, Durham, NH 03824, USA
[9] Solar-Terrestrial Environment Laboratory, Nagoya University, Nagoya 464-8601, Japan
Received 2014 April 21; accepted 2014 June 1; published 2014 July 10

ABSTRACT

The *Interstellar Boundary Explorer* (*IBEX*) returned its first five years of scientific observations from 2009 to 2013. In this study, we examine, validate, initially analyze, and provide to the broad scientific community this complete set of energetic neutral atom (ENA) observations for the first time. *IBEX* measures the fluxes of ENAs reaching 1 AU from sources in the outer heliosphere and most likely the very nearby interstellar space beyond the heliopause. The data, maps, and documentation provided in this study represent the fourth major release of the *IBEX* data, incorporate important improvements, and should be used for future studies and as the citable reference for the current version of the *IBEX* data. In this study, we also examine five years of time evolution in the outer heliosphere and the resulting ENA emissions. These observations show a complicated variation with a general decrease in ENA fluxes from 2009 to 2012 over most regions of the sky, consistent with a 2–4 year recycle time for the previously decreasing solar wind flux. In contrast, the heliotail fluxes continue to decrease, again consistent with a significantly more distant source in the downwind direction. Finally, the Ribbon shows the most complicated time variations, with a leveling off in the southern hemisphere and continued decline in the northern one; these may be consistent with the Ribbon source being significantly farther away in the north than in the south. Together, the observations and results shown in this study expose the intricacies of our heliosphere's interaction with the local interstellar medium.

Key words: local interstellar matter – solar wind – Sun: activity – Sun: heliosphere – Sun: magnetic fields

Online-only material: color figures

1. INTRODUCTION

The *Interstellar Boundary Explorer* (*IBEX*) is the first, and thus far only, mission dedicated to imaging and understanding the interaction of our heliosphere with the local interstellar medium (LISM; see McComas et al. 2009a and other papers in the *IBEX* Special Issue of *Space Science Reviews*). *IBEX* was launched on 2008 October 19, and after roughly two months of orbit raising to place it into its initial highly elliptical orbit (apogee ~50 Earth radii; McComas et al. 2009a; Scherrer et al. 2009), began returning the first global observations of this interaction through measurements of energetic neutral atoms (ENAs).

IBEX measures ENAs in eight energy bins from ~0.1 to 2 keV with *IBEX*-Lo (Fuselier et al. 2009a) and five energy bins from ~0.5 to 5 keV with *IBEX*-Hi (Funsten et al. 2009a). Over six months, ENAs are collected into sets of all-sky maps at all of these different energies. These observations led to the first measurements of the globally distributed ENA flux that was anticipated by various theories and models and to the discovery of a completely unpredicted "Ribbon" of enhanced ENA emissions. These important results from *IBEX* were published in a special issue of *Science* in 2009 November (McComas et al. 2009c; Fuselier et al. 2009b; Funsten et al. 2009b; Schwadron et al. 2009) along with the first direct observation of interstellar H and O neutral atoms, also provided by *IBEX* (Möbius et al. 2009). Table 1 enumerates *IBEX*'s major "firsts" and discoveries over the first five years of science operations along with their original and/or primary reference(s).

Perhaps the most surprising of all of the *IBEX* discoveries is that of the Ribbon. Briefly, the Ribbon is narrow (~20° wide from 0.7 to 2.7 keV; Fuselier et al. 2009b), has ENA fluxes up to ~2–3 times that of the surrounding globally distributed flux (McComas et al. 2009c), is extremely circular (Funsten et al. 2009b, 2013), and appears to be ordered by the external magnetic field in the very LISM (McComas et al. 2009c; Schwadron et al. 2009). McComas et al. (2012b) showed that dominant energies of the Ribbon ENAs as a function of ecliptic latitude very closely follow the latitude-dependent energy distribution of the out-flowing solar wind over the past, protracted solar minimum (McComas et al. 2008, 2013a). This connection strongly indicates that the ultimate source of the Ribbon is directly related to the supersonic solar wind itself.

While there are over a dozen different ideas, scenarios, and models for how the Ribbon ENAs may be generated, much recent evidence, including the latitude dependence of their peak energies, is making some sort of "secondary ENA" generation process seem most likely. Secondary ENAs are generated from solar wind and inner heliosheath ions that become neutralized and radiate out into the other heliosheath only to be re-ionized and trapped on interstellar magnetic field lines, and finally charge exchange again, producing secondary ENAs that can

Table 1
Major "Firsts" and Discoveries over *IBEX*'s First Five Years

Global Heliosphere	
(1) Discovery of an enhanced ENA Ribbon and its connection to the interstellar magnetic field.	McComas et al. 2009c; Fuselier et al. 2009b; Funsten et al. 2009b; Schwadron et al. 2009
(2) First observations of globally distributed ENAs from the inner heliosheath.	McComas et al. 2009a; Schwadron et al. 2009
(3) Discovery of rapid (~6 months) time variations in the heliosphere's interstellar interaction and connection to decreasing solar wind output.	McComas et al. 2010; Reisenfeld et al. 2012; McComas et al. 2012b
(4) Discovery of solar wind-like latitude/energy ordering of Ribbon emissions	McComas et al. 2012b
(5) First observations of the heliotail, its ordering by fast and slow solar wind, and the influence of the interstellar magnetic field on it.	Schwadron et al. 2011; McComas et al. 2013b
Interstellar Medium	
(6) Discovery of our Sun's slower motion and different direction with respect to the interstellar medium.	Möbius et al. 2012; Bzowski et al. 2012a
(7) Discovery that the heliosphere is very likely to have a bow wave ahead of it instead of a bow shock.	McComas et al. 2012a
(8) First direct observations of interstellar Hydrogen, Oxygen, and Neon.	Möbius et al. 2009; Bochsler et al. 2012
(9) First direct detection of interstellar Deuterium.	Rodriguez et al. 2013
(10) Discovery that flow direction in the very local interstellar medium is likely changing in the vicinity around the heliosphere.	Frisch et al. 2013
(11) First connection of LISM environment from *IBEX* to TeV cosmic rays.	Schwadron et al. 2014
Terrestrial Magnetosphere	
(12) First images of the magnetospheric cusps and sub-solar magnetosheath from outside.	Fuselier et al. 2010; Petrinec et al. 2011
(13) First ENA images of the shape of the Earth's plasma sheet and a possible disconnection event.	McComas et al. 2011b
Moon	
(14) Discovery of neutralized and backscattered solar wind from the Moon.	McComas et al. 2009b
Space Mission Capabilities	
(15) First use of additional Solid Rocket Motor on Pegasus LV and spacecraft propulsion to achieve very high altitude orbit.	McComas et al. 2009a; Scherrer et al. 2009
(16) Discovery and first use of long-term stable lunar synchronous orbit.	McComas et al. 2011a

preferentially radiate back inward toward the Sun (and *IBEX*; McComas et al. 2009c). More detailed models and calculations produce very Ribbon-like ENA fluxes if the ENAs are able to stay in ring-beam distributions for the typically few years required to re-neutralize for the last time in the outer heliosheath (Heerikhuisen et al. 2010; Chalov et al. 2010) or if the physical processes, such as scattering and wave–particle interactions of these ions, cause them to be spatially confined (Schwadron & McComas 2013). An early review (McComas et al. 2011b) summarized many of the *IBEX* results from the mission's first two years; most recently, both the observables and the numerous possible Ribbon source mechanisms were examined in a detailed review paper (McComas et al. 2014).

Time variations between the six-month global ENA maps measured by *IBEX* have been examined over the first year of observations (McComas et al. 2010) and first three years of observations (McComas et al. 2012b). In addition, two other studies examined ENA fluxes from the polar regions, which are sampled essentially continuously by *IBEX* and thus have the potential to reveal time variations even more rapid than six months (Reisenfeld et al. 2012; Allegrini et al. 2012). All of these studies, however, showed consistent results with the fastest variations in the global ENA flux being on timescales of six months or longer and indicate a general reduction in the ENA fluxes, qualitatively consistent with the diminishing solar wind output (McComas et al. 2008, 2013a). The most complete study of time variations over the entire sky to date (McComas et al. 2012b) showed the heliospheric ENA emissions both within the *IBEX* Ribbon and outside in the globally distributed flux decreasing from 2009 to 2011 with the Ribbon fluxes decreasing by the largest fraction (~10%–20%, depending on energy, over the three years).

Table 2
Data Intervals Used in First Five Years of IBEX Maps

Year (Annual Maps)	Six-month Maps	Orbit/Arc Numbers	Dates (Start/End of Orbits or Arcs)
Year 1 (2009 Map)	1	11–34	12/25/2008–06/25/2009
	2	35–58	06/25/2009–12/25/2009
Year 2 (2010 Map)	3	59–82	12/25/2009–06/26/2010
	4	83–106	06/26/2010–12/26/2010
Year 3 (2011 Map)	5	107–130a	12/26/2010–06/25/2011
	6	130b–150a	06/25/2011–12/24/2011
Year 4 (2012 Map)	7	150b–170a	12/24/2011–06/22/2012
	8	170b–190b	06/22/2012–12/26/2012
Year 5 (2013 Map)	9	191a–210b	12/26/2012–06/26/2013
	10	211a–230b	06/26/2013–12/26/2013

This study extends the work of McComas et al. (2012b) and provides the documentation for the release of *IBEX* ENA observations from the mission's fourth and fifth years (2012 and 2013) for the first time, as well as the re-release, with slightly improved background subtraction and correction factors, of years one through three (2009–2011). Section 2 shows the five years of data in various forms. In Section 3, we examine time variations of the ENA flux observed by *IBEX* over nearly half a solar cycle of data and in Section 4 we discuss the implications of the additional new observations and the developing understanding of the heliosphere's interaction with the LISM. The Appendices provide detailed documentation for several small improvements in the data correction and processing. This study extends and improves the time variable cosmic ray background correction (Appendix A) and orbit-by-orbit survival probability corrections (Appendix B) introduced by McComas et al. (2012b). In addition, we examine the possibility of a time variable efficiency factor for *IBEX*-Hi (Appendix C) and include for the first time corrections in *IBEX*-Hi data for a small residual background produced by the "ion gun" effect inside the instrument (Appendix D). Finally, Appendix E describes a new correction for contamination of *IBEX*-Lo data by sputtering of higher energy ENAs and interstellar neutrals within that instrument. This study should be used as the citable reference for the first five years of *IBEX* data and for the corrections to and validation of the best possible data set that the *IBEX* team can currently provide. These data are available at: http://ibex.swri.edu/researchers/publicdata.shtml, are also reachable through the data section of the general *IBEX* Web site: http://ibex.swri.edu/, and can be found in the archive at the National Space Science Data Center (NSSDC): http://nssdc.gsfc.nasa.gov/.

2. FIVE YEARS OF *IBEX* OBSERVATIONS

IBEX is an ∼4 rpm Sun-pointed spinning spacecraft (McComas et al. 2009a) with two single pixel ENA cameras, *IBEX*-Hi (Funsten et al. 2009a) and *IBEX*-Lo (Fuselier et al. 2009a), viewing perpendicular to the spin axis. This geometry allows imaging of ENAs coming in from a fixed (great circle) band around the sky over each spacecraft spin. Over orbits 128 and 129, we adjusted *IBEX*'s orbital period from ∼7.5 days to ∼9.1 days, and placed it into a long-term stable lunar synchronous orbit with apogee still ∼50 R_E (McComas et al. 2011a). This change necessitated a modification to operations starting with orbit 130, with repointing of the spacecraft toward the Sun both near perigee and apogee instead of just once per orbit near perigee. We designate these orbit arcs "a" (ascending) and "b" (descending), respectively, and they provide observational "swaths" of sky viewing ∼4.°5, instead of the prior ∼7.°5, apart. With either repointing scheme, the spacecraft rotates the band of observations through 180° and *IBEX* captures a complete set of energy-resolved sky maps over the course of each six-month interval. Table 2 provides the dates and orbit/orbit arc numbers for all 10 energy-resolved sets of six-month and annual maps; the first six map intervals (three years) are the same as in McComas et al. (2012b).

Table 3
IBEX-Hi Energy Pass Bands (Qualified Triple-Coincidences)

ESA step	E_{-HM} (keV)	E_{nom} (keV)	E_{+HM} (keV)	$\Delta E/E$
2	0.52	0.71	0.95	0.60
3	0.84	1.11	1.55	0.63
4	1.36	1.74	2.50	0.66
5	1.99	2.73	3.75	0.64
6	3.13	4.29	6.00	0.67

In orbit segment 184a, we made an additional change to the *IBEX* operations and modified the sequence of six energy steps in *IBEX*-Hi from ESA 1–2–3–4–5–6 to 2–3–3–4–5–6. This modification removed the lowest ESA step, which often had too much background to be scientifically useful, in exchange for a doubling of the statistical sampling of ESA 3 (center energy ∼1.1 keV), where the *IBEX* ribbon is most pronounced. Table 3 shows the energy pass bands of the ESAs 2–6 from *IBEX*-Hi used in this study. Observations shown in this study, starting in segment 184a, include the doubled viewing time and improved counting statistics at the ESA 3 energy.

2.1. *IBEX* ENA Data Processing

Just as for the McComas et al. (2012b) paper, the *IBEX*-Hi flux maps are based on the most reliable triple coincidence events that occur within a 96 ns time window (Funsten et al. 2009a). Also as done in our prior study, we have culled out *IBEX*-Hi times of enhanced background and/or poor data, including times with high count rates in the *IBEX* Background Monitor (Allegrini et al. 2009); apparent enhancements in ENA fluxes at lower energies over wide spin phases; times when the Earth, Moon, or Earth's magnetosphere are in the field of view; enhancements from solar energetic particle events; and rare count bursts that were also observed during instrument calibration and whose coincidence combinations are definitively not ENAs. The data

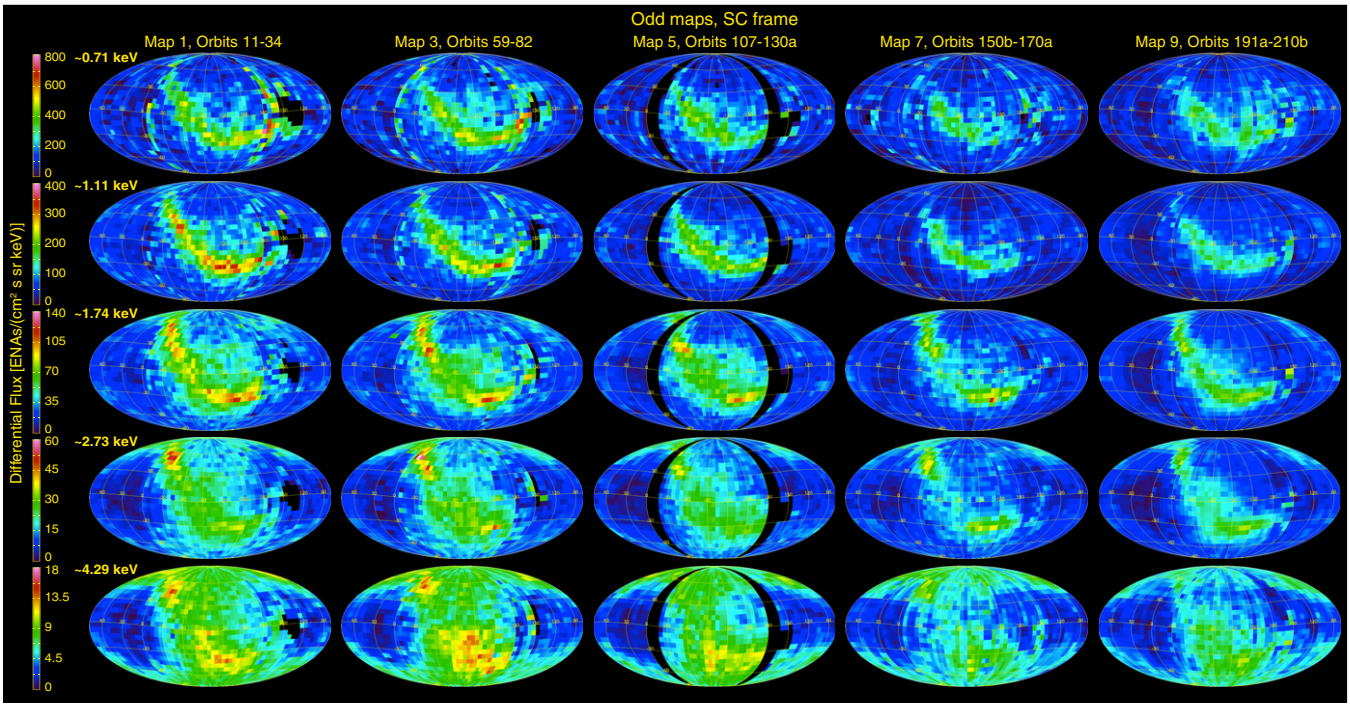

Figure 1. Mollweide projections of odd numbered *IBEX*-Hi ENA flux maps (columns) for five different energy pass bands (rows). Color bars are fixed for all maps at each of the five *IBEX*-Hi energies throughout this study. Black regions indicate no data; missing arcs in Map 5 are from when we were maneuvering *IBEX* into a long-term stable, lunar synchronous orbit (McComas et al. 2011a).

(A color version of this figure is available in the online journal.)

set here includes culling for the new years 4 and 5 and provides slightly improved culling for a few orbits in years 1–3.

The new five year data set provided here also includes a slightly improved correction for the time variable cosmic ray background for the first three years as well as its extension through years 4 and 5 (Appendix A), new orbit-by-orbit survival probability corrections for some orbits of year 3 as well as years 4 and 5 (Appendix B), and re-examines the possibility of a time variable efficiency factor (Appendix C). Also new for this study, we include corrections for a residual background produced by the "ion gun" effect inside *IBEX*-Hi (Appendix D). The ion gun background is generated by acceleration of ions produced by electron impact ionization of neutral atoms and molecules within *IBEX*-Hi and thus is sensitive to the number of electrons entering the sensor and available to ionize any residual gas (Wurz et al. 2009). Finally, as done in McComas et al. (2012b), we include times after subtracting a small additional isotropic background for orbits where statistics are low; this process improves the statistical accuracy of otherwise poorly resolved swaths.

IBEX-Lo data used in this study include *IBEX*-Lo's top four energy pass bands (5–8) of Fuselier et al. (2009b), which cover the range from 0.15 to 2.6 keV (FWHM). The culling procedure for *IBEX*-Lo year 4 and 5 data is similar to that of *IBEX*-Hi and generally the same as used previously in our three-year study (McComas et al. 2012b). Details of the *IBEX*-Lo map processing are described in Fuselier et al. (2012). In addition, for the first time, we remove an additional background produced inside *IBEX*-Lo by the sputtering of neutrals (Appendix E).

2.2. IBEX-Hi Maps in the Spacecraft Frame

Unless otherwise stated, *IBEX* ENA observations in this study are shown in *IBEX* standard Mollweide projections—centered toward the direction of the incoming interstellar flow with respect to the heliosphere. In contrast to our prior three-year study (McComas et al. 2012b), in this study we center the maps on ecliptic longitude and latitude ($\lambda_{ISM\infty}$, $\beta_{ISM\infty}$) of (79.°0, −5.°0) (McComas et al. 2012a). This direction is slightly revised and improved from the one previously used for centering all prior *IBEX* maps, which was provided by earlier observations from the Ulysses mission (Witte 2004). Figures 1 and 2 show the ENA fluxes observed by *IBEX*-Hi in the odd (1, 3, 5, 7, 9) and even (2, 4, 6, 8, 10) sets of maps, respectively. In order to aid in comparison between various figures, we use the same color bars for each energy pass band across all of the various figures throughout this study.

Earth's orbital motion about the Sun (~30 km s^{-1}) produces significant alterations in both ENA energy and velocity vector that appears as a systematic flux variation in the maps in Figures 1 and 2. This Compton-Getting (C-G) effect is produced by the spacecraft motion with respect to the incoming ENAs. As shown in Figure 4 of McComas et al. (2012a), because the spacecraft is ramming into ENAs, the regions around the center (sides) of the Mollweide maps show enhanced (reduced) fluxes of ENAs in the odd numbered maps and the opposite in the even numbered maps. This C-G effect also changes the energies of the ENAs that are measured in each energy pass band, with lower energies sampled on the ram side and higher energies on the anti-ram. Finally, the C-G effect is most noticeable at low energies and is latitude (spacecraft spin-angle) dependent, with the largest energy/magnitude changes at low latitudes and largest direction changes at high latitudes.

2.3. IBEX-Hi Maps in the Inertial Frame

We correct the *IBEX* data in both energy and angle for the C-G effect using the fluxes measured at various energies and following the procedure described in the Appendix of McComas et al. (2010) and slightly modified in McComas et al. (2012b). Figures 3 and 4 show the odd and even C-G corrected maps,

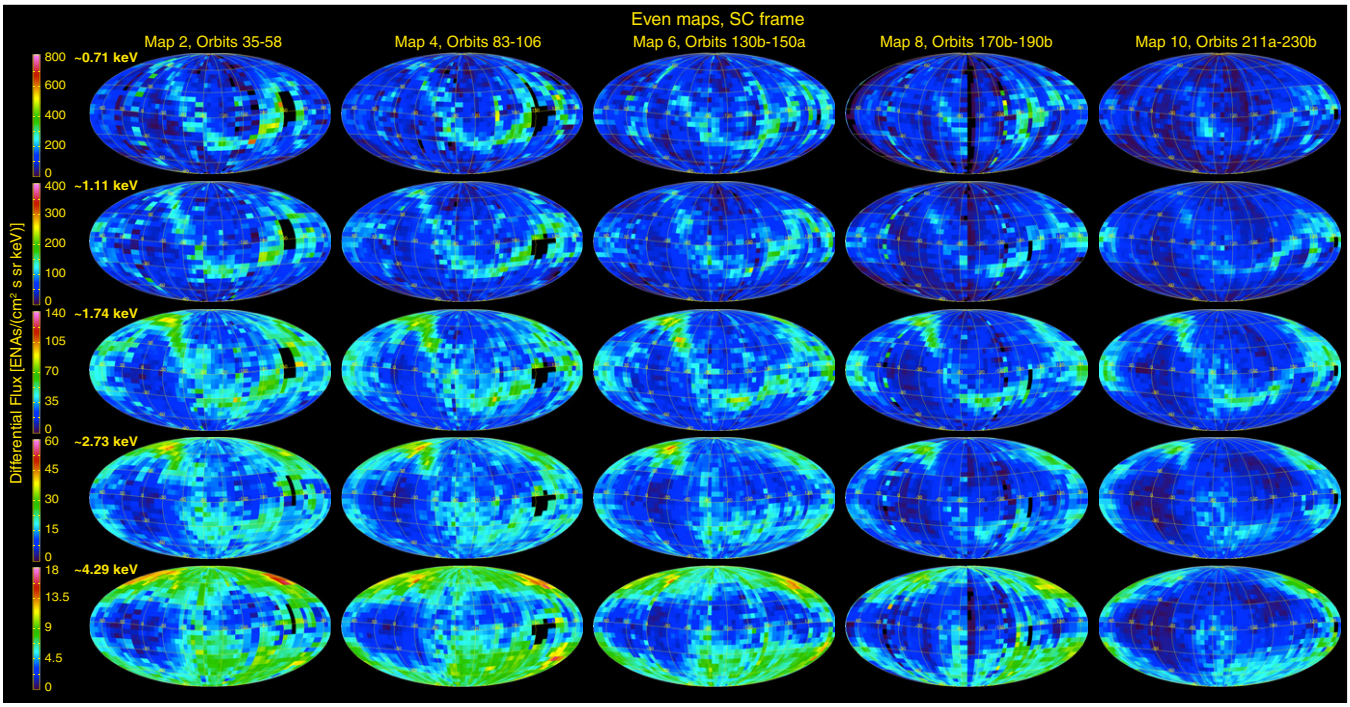

Figure 2. Same as for Figure 1, but for even numbered maps.
(A color version of this figure is available in the online journal.)

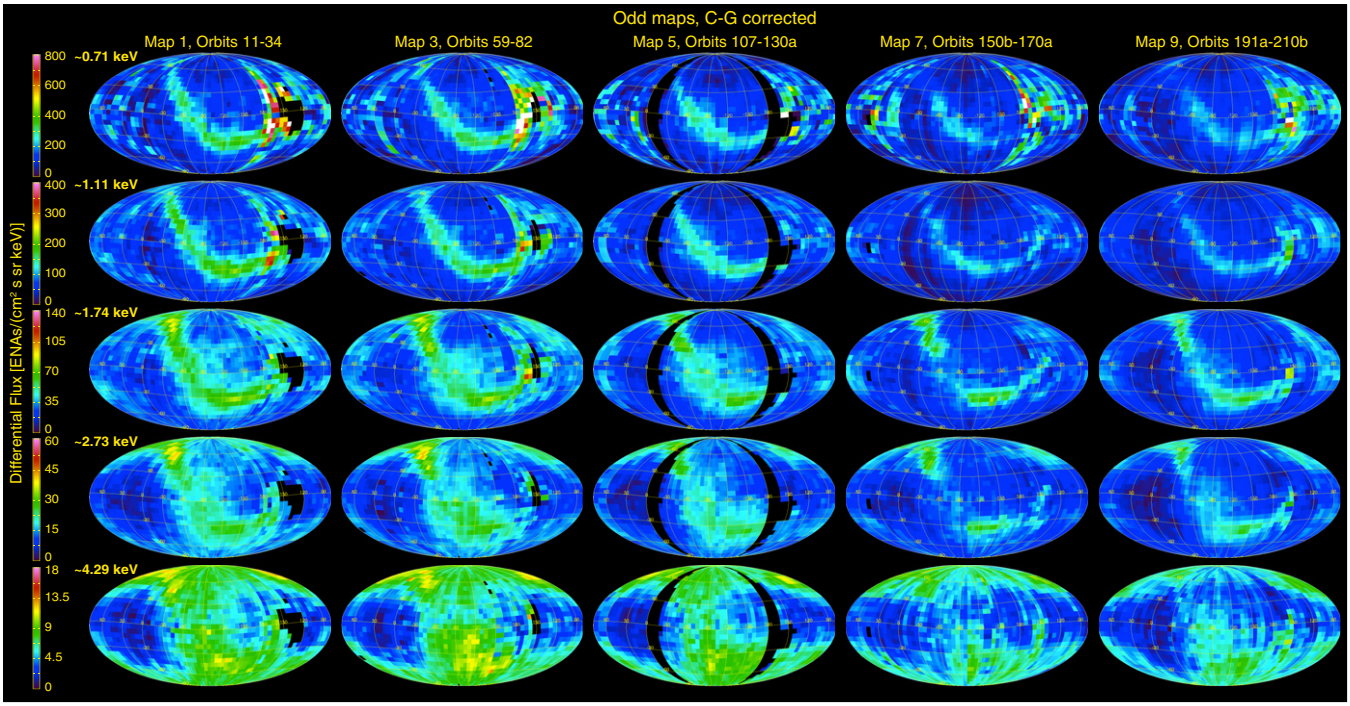

Figure 3. Odd ENA maps as in Figure 1, but C-G corrected into the heliospheric reference frame.
(A color version of this figure is available in the online journal.)

respectively. While there are a number of advantages to using the C-G corrected *IBEX* maps, we caution that they represent inferred ENA fluxes rather than the direct observations and thus may contain artifacts created by the correction process. Thus, we do not use these maps for any studies of time variations in the observed ENAs (see below).

One advantage of C-G corrected maps is that all pixels represent the same energy ENAs, so odd and even maps can be combined together into a single, highly statistically significant product. Figure 5 shows the maps for the five *IBEX*-Hi energy steps, produced by combining all 10 maps produced in *IBEX*'s first five years of observations. These sky maps currently represent the "best" average ENA flux measurements observed at ∼1 AU, in the heliospheric reference frame. As we did for the earlier three-year combined results, the *IBEX* team now recommends using the results shown in Figure 5 of this study for comparison with models and theories seeking to explain the ENA fluxes at 1 AU for the *IBEX*-Hi energy energies.

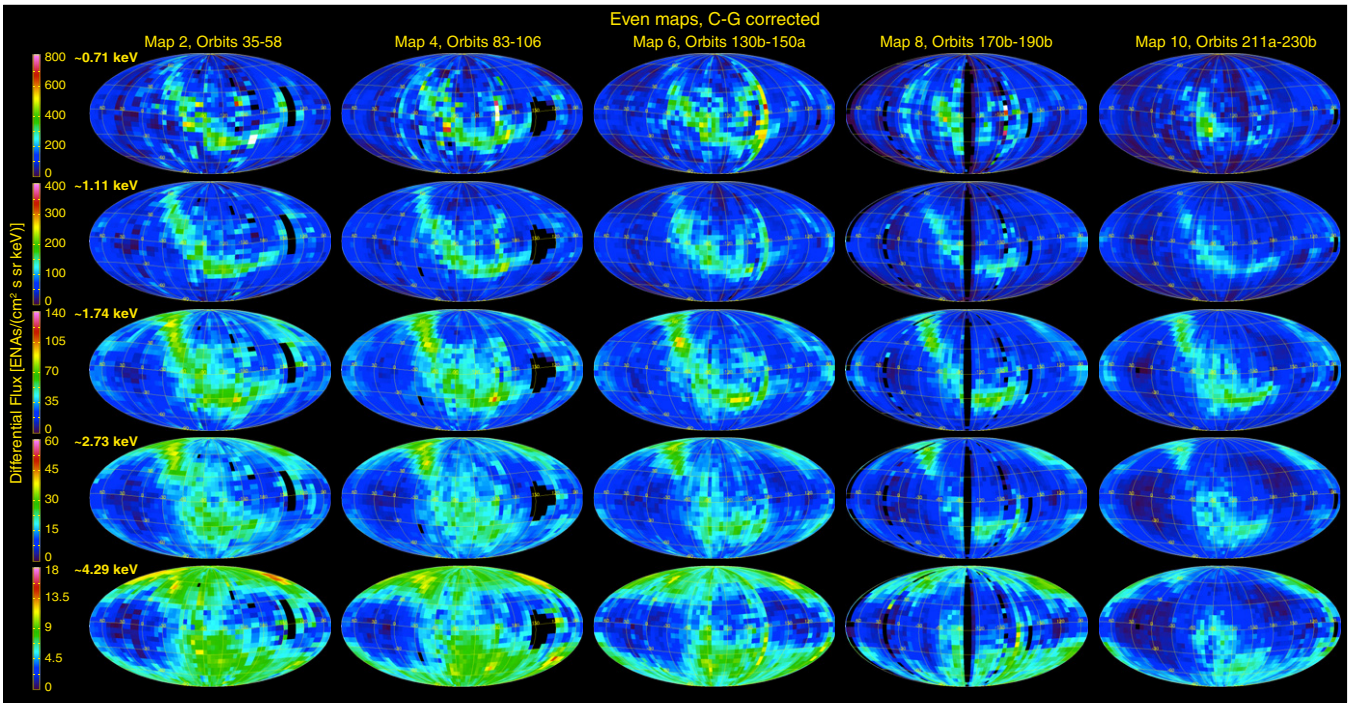

Figure 4. Same as for Figure 3, but for the even numbered ENA maps. Regions of insufficient data (black) differ slightly from Figure 2 owing to how various orbits' data are combined to produce the maps.

(A color version of this figure is available in the online journal.)

2.4. IBEX Maps with Survival Probability Correction

Our three-year study introduced a detailed process for correcting the ENA fluxes observed by *IBEX* at 1 AU for losses owing to ionization of ENAs transiting in from the outer heliosphere (McComas et al. 2012b). This survival probability correction is energy-dependent, heliolatitude-dependent, and time variable as the Sun and solar wind vary. The correction we developed includes radiation pressure and the loss of ENAs from both photoionization and charge exchange with the solar wind protons; both of these losses are greatest within the innermost few AU of the Sun. Appendix B documents the orbit-by-orbit survival probabilities used in this study, including the new orbits that comprise years 4 and 5 of the *IBEX* data, for both the *IBEX*-Hi and *IBEX*-Lo energy pass bands; lower energy ENAs are especially sensitive to this correction as an increasing fraction of the incoming ENAs are lost at lower energy.

Figure 6 shows a sample of the calculated survival probabilities for the northern (top) and southern (bottom) polar pixels for *IBEX*-Hi ESA levels 2–6. The red points were used in McComas et al. (2012b), while the blue ones are used in this study. Previously extrapolated values (red circles) have been adjusted to slightly (∼1%) lower values with the inclusion of new data, while all other prior values are identical or only very slightly improved. The extrapolation for the current study is shown by the cyan squares. It is interesting to note that while the survival probabilities have started going back up in the last couple years in the northern polar pixel, they continue to decrease, or at best flatten out, in the southern one. Clearly these sorts of detailed orbit-by-orbit and pixel-by-pixel corrections are critical to inferring the correct source fluxes generated in the outer heliosphere and beyond.

IBEX-Hi maps that include the survival probability corrections (as well as C-G correction) are shown in Figures 7 (odd orbit numbers), 8 (even orbit numbers), and 9 (all 10 orbits combined together). This last set of 10 orbit combined maps provide the *IBEX* team's current best observations as to the likely fluxes of inward directed ENAs in the outer heliosphere (but inside the region where they are generated) before ionization losses occur in transit to their observation location at 1 AU; these data should be used by the theory and modeling communities which seek to match up with *IBEX* ENA measurements without including the complexities of ENA losses inside of tens of AU.

2.5. IBEX-Hi Ram and Anti-Ram Maps

Other sky maps introduced for the first time by McComas et al. (2012b) were the annual ram and anti-ram maps. For these, data from an entire year of observations are combined at each energy step to produce two separate maps. Ram maps are produced using data from the spin phases in the ram (or spacecraft velocity vector) hemisphere, while anti-ram maps are produced from data in the anti-ram (opposite the velocity vector) hemisphere. While these maps still sample different energies at different ecliptic latitudes, they do not require C-G corrections to be directly compared from one year to the next as each pixel in the sky measures the same exact energies and angles from year to year. This has huge advantages for examination of time variations without the additional (and unknown) errors introduced by C-G corrections. We note, however, that in order to compare data from different years, the fluxes do need to be corrected for survival probability as the ENA losses in the inner heliosphere vary over time. Thus, the annual ram and anti-ram maps can be compared to other ram and anti-ram maps, respectively, on a pixel-by-pixel basis with only statistical and survival probability correction errors to contend with. Figures 10 and 11 show the ram and anti-ram maps for years 2009–2013, respectively; Figures 12 and 13 show the five year combined maps for the ram and anti-ram directions. For all four figures, survival probability corrections have been included, but not C-G corrections.

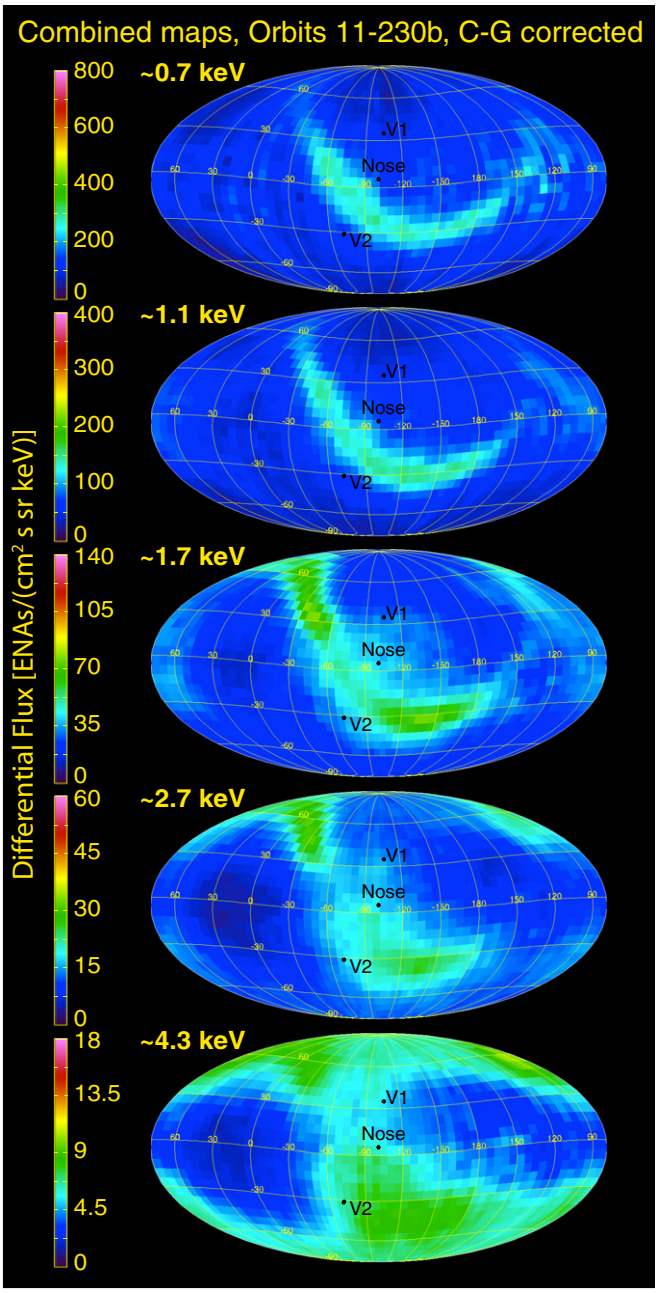

Figure 5. ENA fluxes from combined maps 1–10 in the heliospheric reference frame. The points indicate locations in the sky maps of the direction of interstellar inflow (center) and *Voyagers 1* and *2* (*V1* and *V2*).

(A color version of this figure is available in the online journal.)

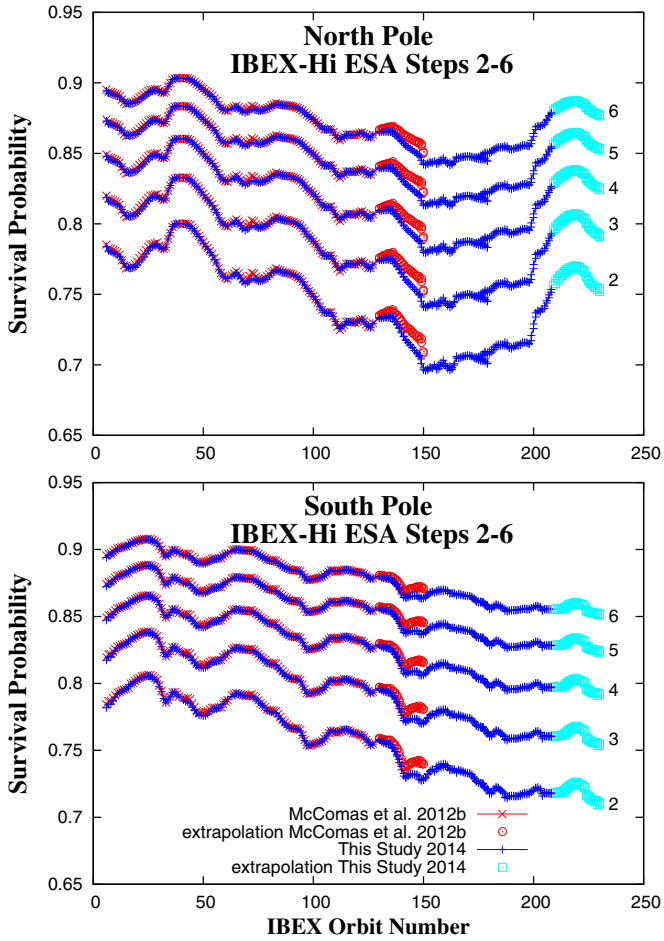

Figure 6. Calculated survival probabilities for ENAs coming in from the outer heliosphere and arriving in *IBEX*'s northern (top) and southern (bottom) polar pixels.

(A color version of this figure is available in the online journal.)

2.6. IBEX-Lo Maps

While this study primarily examines the *IBEX*-Hi data, as we did in the earlier three-year study, we also include *IBEX*-Lo maps for energies from ∼0.2 to 1.8 keV. Figure 14 provides the updated *IBEX*-Lo maps, including the observations from all five years and a new correction to remove apparent signal from sputtering of ENAs and interstellar neutrals within *IBEX*-Lo (Appendix E). The left column shows the uncorrected *IBEX*-Lo maps in the spacecraft frame, while the right column gives the same data, but including corrections for the survival probability of outer heliospheric ENAs making it into 1 AU. This study is also the first to include survival probabilities for *IBEX*-Lo sky maps and we note that these corrections can be quite large at the lowest energies.

While the *IBEX*-Lo data clearly have lower statistical significance than *IBEX*-Hi, the two higher energy maps are important because they continue to provide independent observations that validate the *IBEX*-Hi observations of the Ribbon at these overlapping energies (McComas et al. 2009c). At the two lower energies, *IBEX*-Lo provides the only measurements of heliospheric ENAs and thus extends the range of measurements of heliospheric ENA fluxes to lower energies. With only the first three years of data, McComas et al. (2012b) said that the Ribbon dims and broadens at 0.2 and 0.4 keV, just as it does at energies above ∼1 keV. With the increased statistical significance of the five years of observations and an additional correction that removes the internal background due to sputtering, we find that the Ribbon may be almost nonexistent by the lowest energy step of ∼0.2 keV. This suggests that much of the Ribbon signature previously identified in the 0.2 keV maps may have been due to sputtering from the higher energy Ribbon ENAs. Here, we find that the ∼0.2 keV ENAs show a quite broad enhancement of low energy emissions centered near the nose, but shifted somewhat toward the upfield longitude (to the right in this figure).

2.7. IBEX-Hi Maps of the Spectral Index

The spectral slopes of the five *IBEX*-Hi energy steps are shown for the ram and anti-ram maps in Figure 15. For each, the fluxes were calculated at each energy step in each pixel

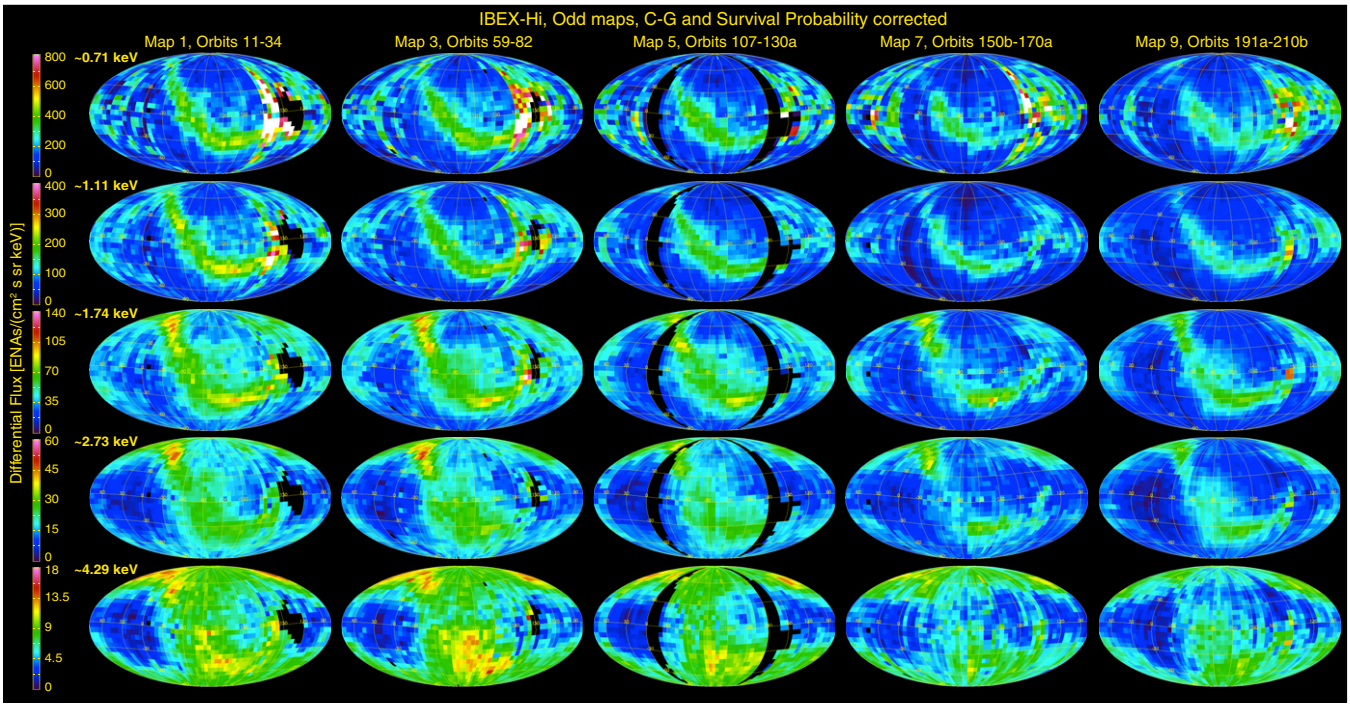

Figure 7. Survival probability and C-G corrected ENA fluxes for the *IBEX*-Hi odd maps (1, 3, 5, 7, 9), which are representative of inward-directed ENA fluxes in the outer heliosphere, before ionization losses during their transport into the inner heliosphere. In a few of the maps the heliospheric viewing time is so low in the region of substantial magnetospheric contamination (black region on right side of maps) that they produce statistically noisy data and unphysically high and variable results; such pixels should be ignored.

(A color version of this figure is available in the online journal.)

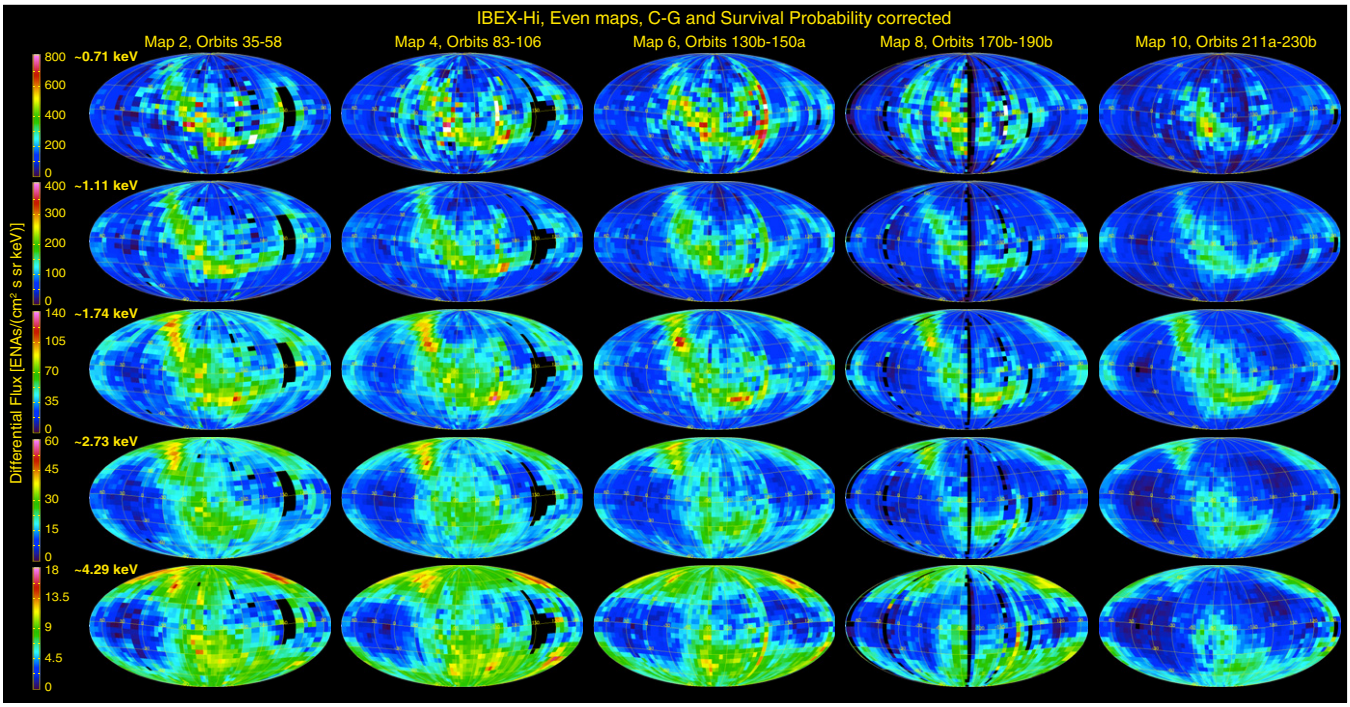

Figure 8. Similar to Figure 7, but for even maps (2, 4, 6, 8, 10).

(A color version of this figure is available in the online journal.)

and the energy spectral index (γ) was calculated to fit to these data points. In order to accurately determine the spectral index, fluxes must first be corrected for the motion of the spacecraft ($\sim$30 km s^{-1}). However, the full CG correction also injects errors owing to the statistical uncertainties of the data and need to fit a slope locally over the (unknown) spectrum. Thus, as we did in McComas et al. (2012b), here we leave the fluxes as measured and simply attribute those fluxes to energy pass bands that have been corrected for the spacecraft motion on a pixel-by-pixel basis. This, much simpler and not model-dependent

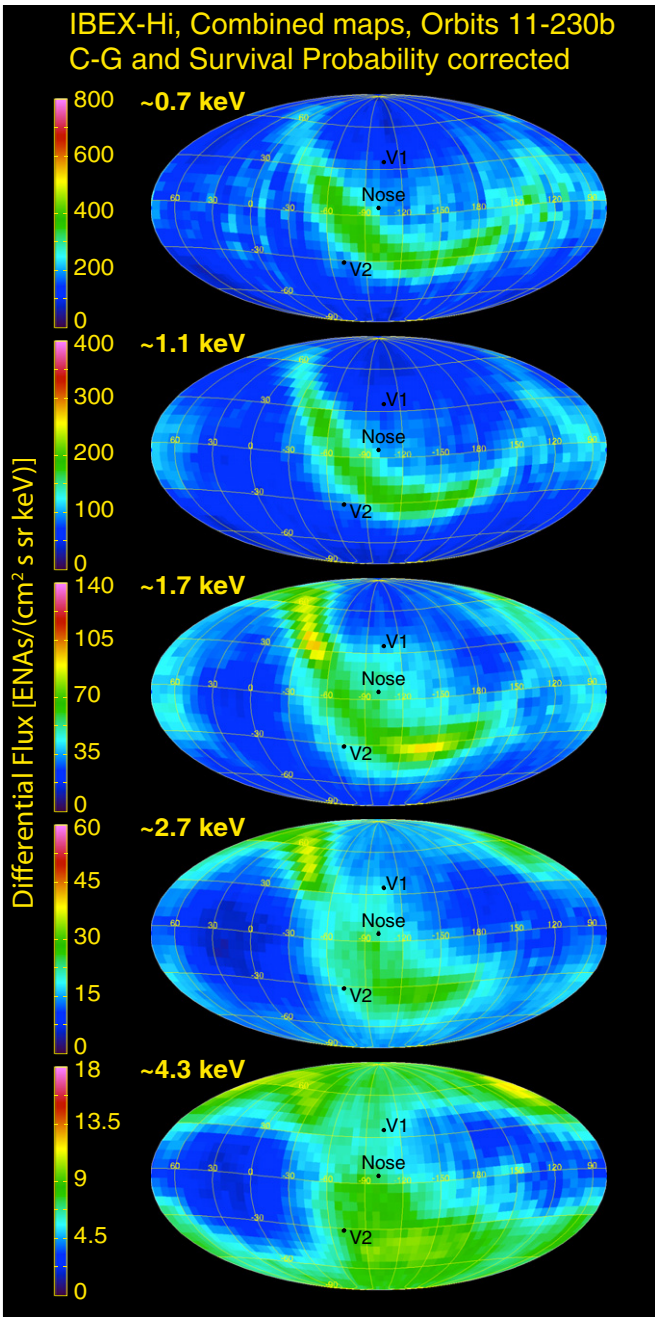

Figure 9. Statically combined survival probability and C-G corrected maps, indicative of ENA fluxes in the outer heliosphere directed inward and before ionization losses. As before, the flux ranges of the color bars are the same as previous maps.

(A color version of this figure is available in the online journal.)

correction effectively puts the observations in the Sun's inertial frame. Figure 16 shows equivalent maps, but also including corrections for the ENA survival probability as a function of energy and time.

The *IBEX* Ribbon is clearly visible in spectral maps, with a spectral index of ~2–2.5, somewhat larger than the surrounding regions which typically have spectral indices $\leqslant 2$. In addition, spectral slopes across the maps, even in the higher latitude regions have indices typically no greater than ~1.5. This number is the limiting, "anti-equilibrium" value for a kappa distribution, where particle distributions are as far from equilibrium as possible (Livadiotis & McComas 2009, 2010, 2013). It is important to note, however, that the *IBEX* energy spectra from high latitudes are less well fit by a single power law than at low to mid latitudes and tend to show an upward inflection around the middle of the *IBEX*-Hi energy (McComas et al. 2009c; Dayeh et al. 2012).

Away from the nose, the spectral index shows larger values, typically >2.5, in two broad regions at low to mid latitudes. While earlier studies based on the first year of *IBEX* data only associated one of these features with a tail for the heliosphere (Schwadron et al. 2011), McComas et al. (2013b) recently examined the first three years of data for this region and showed that the two regions represent port and starboard "lobes" of a large heliotail structure that is centered in nearly the downwind direction.

2.8. Different Map Views Highlight Different Results

One of the lessons learned from the heliotail study (McComas et al. 2012b) was the importance of looking at the *IBEX* data from different perspectives. To date, almost all published *IBEX* Mollweide projections have been centered on the upwind (nose) direction through the interstellar medium, with older plots centered on the Ulysses-derived direction (Witte 2004) and newer plots, including the ones so far in this paper, centered on the improved upwind direction vector (McComas et al. 2012a). Figure 17 shows combined ram maps as a function of energy for the full five year data set, but centered on the downwind direction—exactly opposite from the *IBEX*-derived upwind direction. In these maps, it is easy to see two regions of very low fluxes of higher energy ENAs (especially in the top two energy steps); these indicate the port and starboard lobes of slow solar wind headed down the heliotail. Similarly, the enhancements in flux at these higher energies north and south of the downwind direction indicate the high speed solar wind heading down the heliotail from higher northern and southern latitudes on the Sun (McComas et al. 2013b).

Additional perspectives are provided in Figures 18 and 19, which give Mollweide projections centered on the *IBEX* Ribbon and presumably external interstellar field direction of (219.2LISM, 39.°9) in ecliptic coordinates, as determined by *IBEX* (Funsten et al. 2013). Figure 18 is centered on the upfield direction (direction of the external field on the upwind side of the heliosphere)—this perspective was first shown by Funsten et al. (2009b) and then used by McComas et al. (2012b) to discover the latitude ordering of the energy dependence of the Ribbon in the first three years of *IBEX* data. As seen in this figure, ribbon emissions are strongest near the ecliptic plane only in the lowest two pass bands, which represent typical low to mid latitude solar wind energies of ~1 keV. In contrast, with increasing energy above this, the Ribbon emissions appear to move to higher and higher latitudes. In the highest pass band (centered on ~4.3 keV) the Ribbon is only strong above ~45°. McComas et al. (2012b) argued that such an association strongly implicates a quite direct recycling of the solar wind ions into Ribbon ENAs, such as that provided by a "secondary ENA" source (McComas et al. 2009c; Heerikhuisen et al. 2010; Schwadron & McComas 2013) or possibly by a termination shock related Ribbon source (e.g., Kucharek et al. 2013).

Figure 19 shows, for the first time, a Mollweide projection of the ENA fluxes centered on the downfield direction (direction of the external field on the downwind side of the heliosphere). In this view, the *IBEX* Ribbon is again centered in these Mollweide projections, however, because it has a half cone angle of only 74.°5 (Funsten et al. 2013) instead of ~90°, it appears beyond the

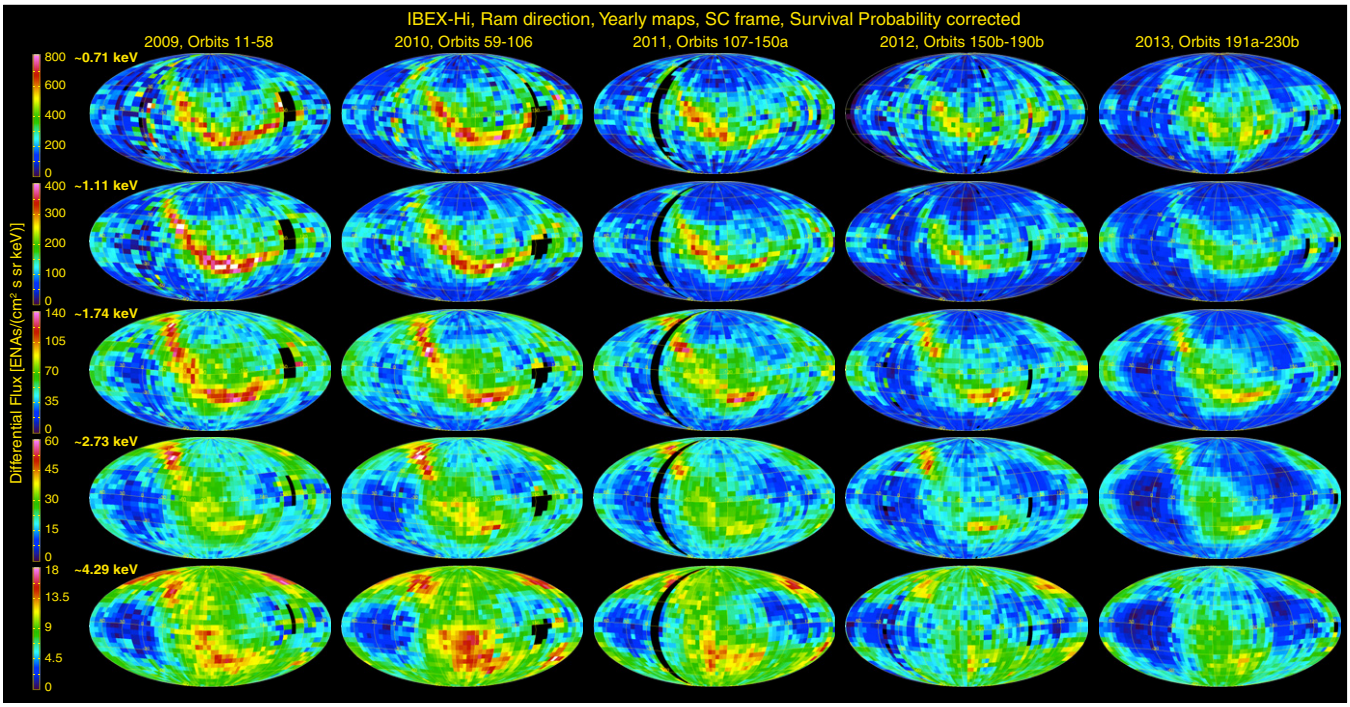

Figure 10. Annual ram maps for 2009–2013 for *IBEX*-Hi, produced by combining observations where the instrument aperture was pointed in the hemisphere of the spacecraft's motion. Fluxes are corrected for ENA survival but not C-G corrected.

(A color version of this figure is available in the online journal.)

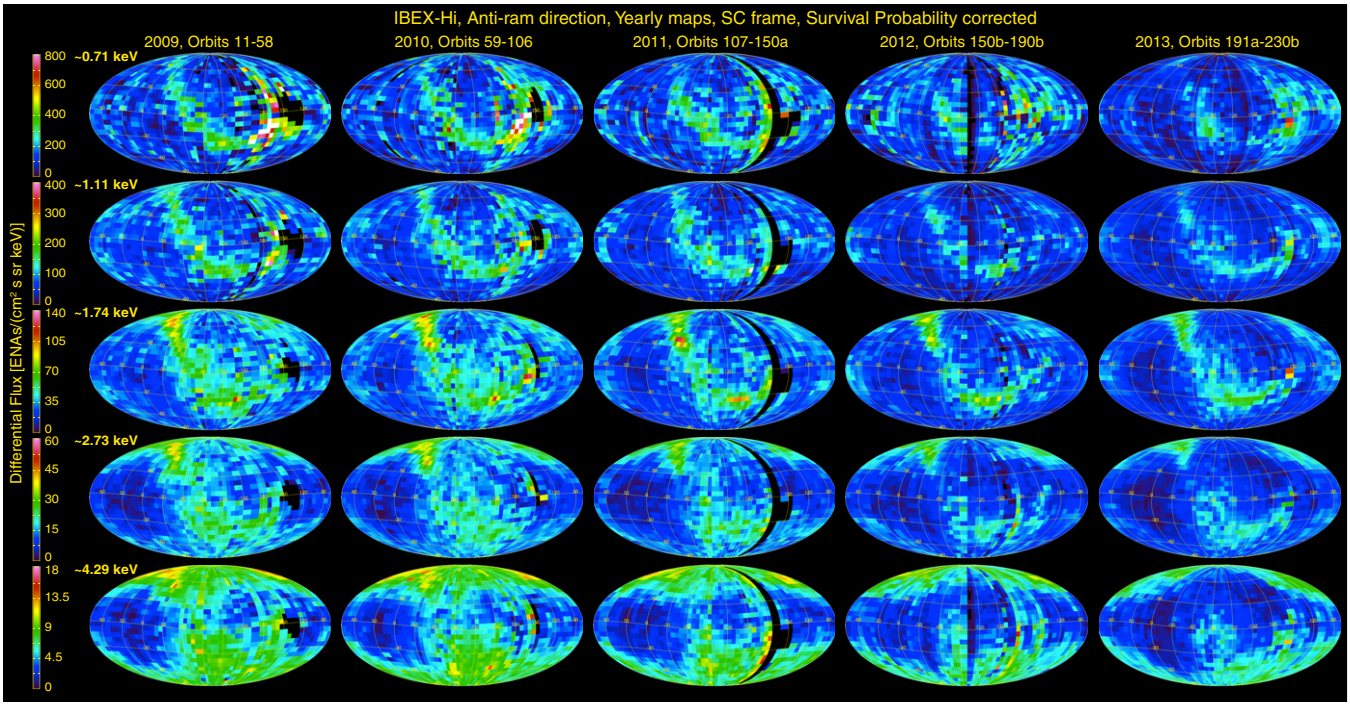

Figure 11. Similar to Figure 10, but "anti-ram" observations.

(A color version of this figure is available in the online journal.)

upwind/downwind terminator. Thus, it appears to emerge from the top and bottom of the plots in this projection, connecting only through the "wrapping" of the projection from one side to the other. Still, the coupling between the solar latitude and energies of the ENA emissions is clear.

Another interesting aspect of the downfield-centered perspective is that the heliotail, especially the slow solar wind lobes (McComas et al. 2013b) as indicated by the dearth of higher energy ENAs, shows a significant asymmetry. Using the Mollweide (constant solid angle) projection, it is apparent that the more nearly downfield (port) lobe is clearly larger than the other (starboard) lobe. This asymmetry in the heliotail reinforces the importance of the external magnetic field in shaping the heliosphere's interstellar interaction (Schwadron et al. 2011;

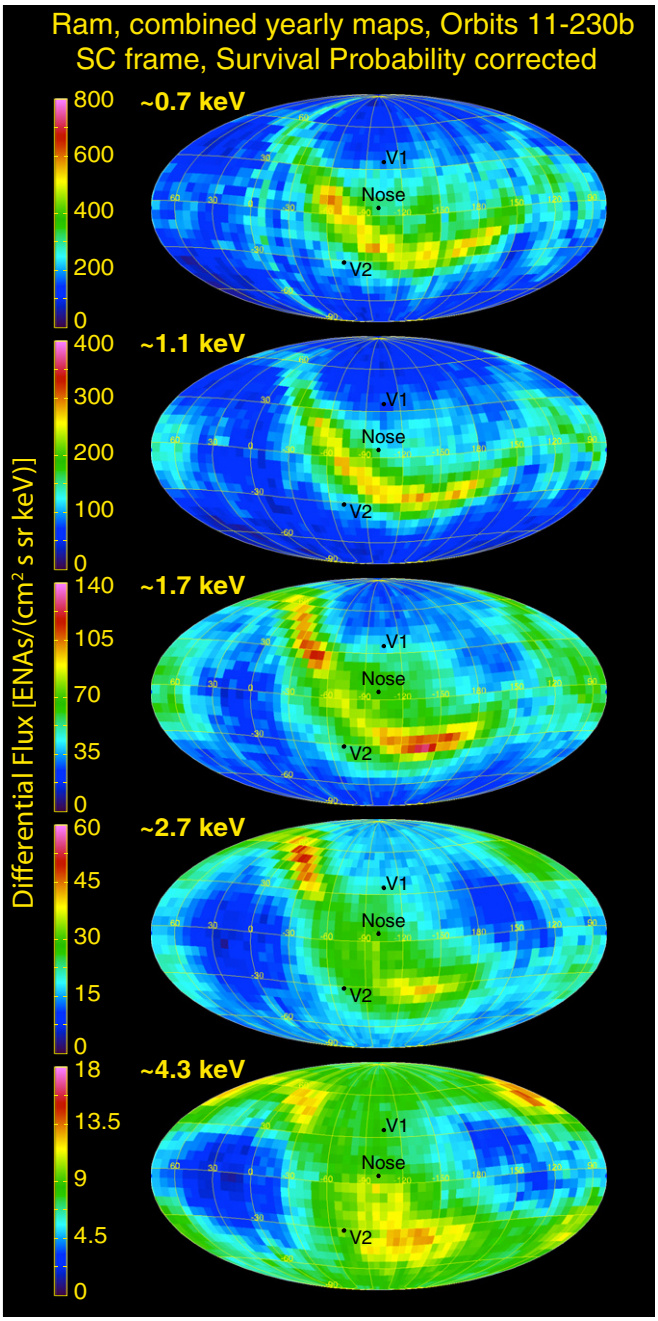

Figure 12. Ram maps produced by statistically combining all five annual ram maps from Figure 10.

(A color version of this figure is available in the online journal.)

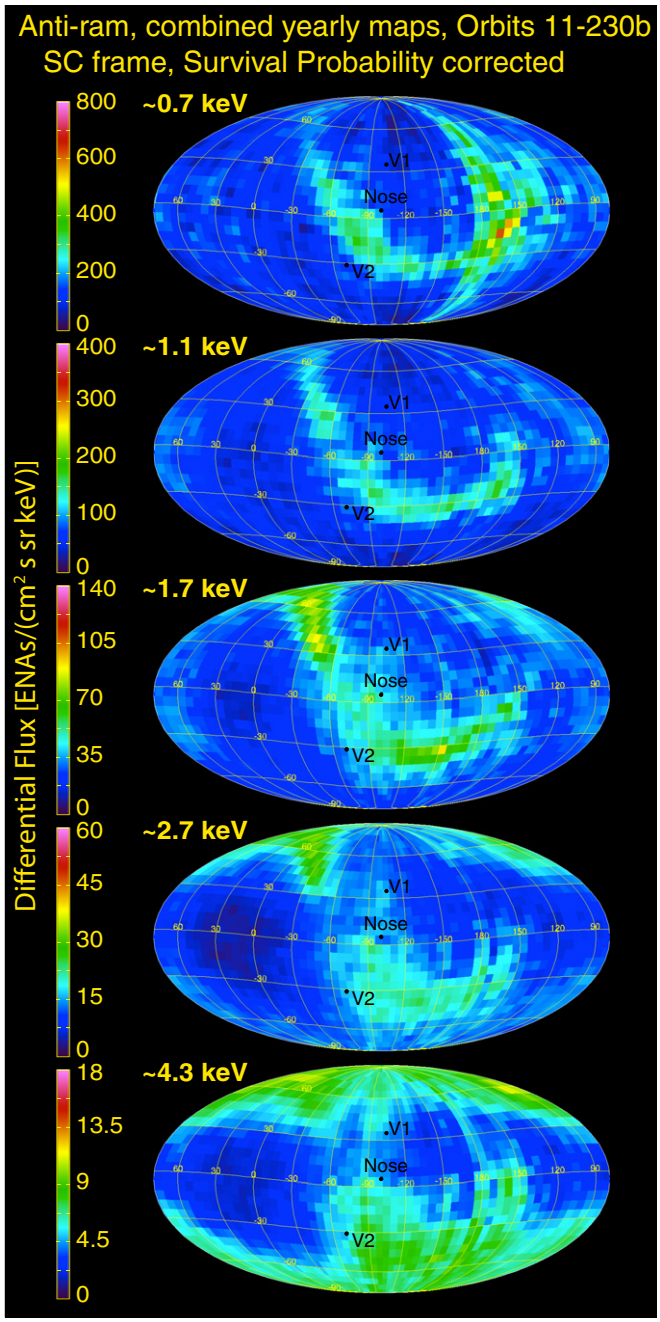

Figure 13. Similar to Figure 12, but anti-ram maps. The brightest pixels and associated arcs at the lowest energy indicate some residual flux when *IBEX* is trying to view past the magnetosphere.

(A color version of this figure is available in the online journal.)

McComas et al. 2013b; Kivelson & Jia 2013) and provides another key observation supporting the relatively unique conditions of the heliosphere's current interaction, where external dynamic and magnetic influences are roughly equally important as suggested, based on the discovery of the Ribbon, by McComas et al. (2009c).

3. TIME VARIATIONS OVER FIVE YEARS OF *IBEX* OBSERVATIONS

This analysis follows on the earlier work McComas et al. (2010), who looked for time variations over *IBEX*'s first year of observations (between Maps 1 and 2), and McComas et al. (2012b), who examined variations over the first three years of *IBEX* data (Maps 1–6). In this study, with five full years of *IBEX* observations (2009–2013), we can examine longer term trends in the ENA fluxes and begin to search for effects of the solar wind's variable structure over its ∼11 year solar cycle. This allows *IBEX* to start resolving the four-dimensional heliosphere—i.e., not just its spatial structure, but as a three-dimensional object varying over time.

As we did in the McComas et al. (2012b) study, here we (1) avoid comparisons of C-G corrected maps, where spectral interpolation injects additional uncertainties in the apparent fluxes, (2) examine fluxes that have been carefully corrected, on an orbit-by-orbit basis, for the survival probability of various

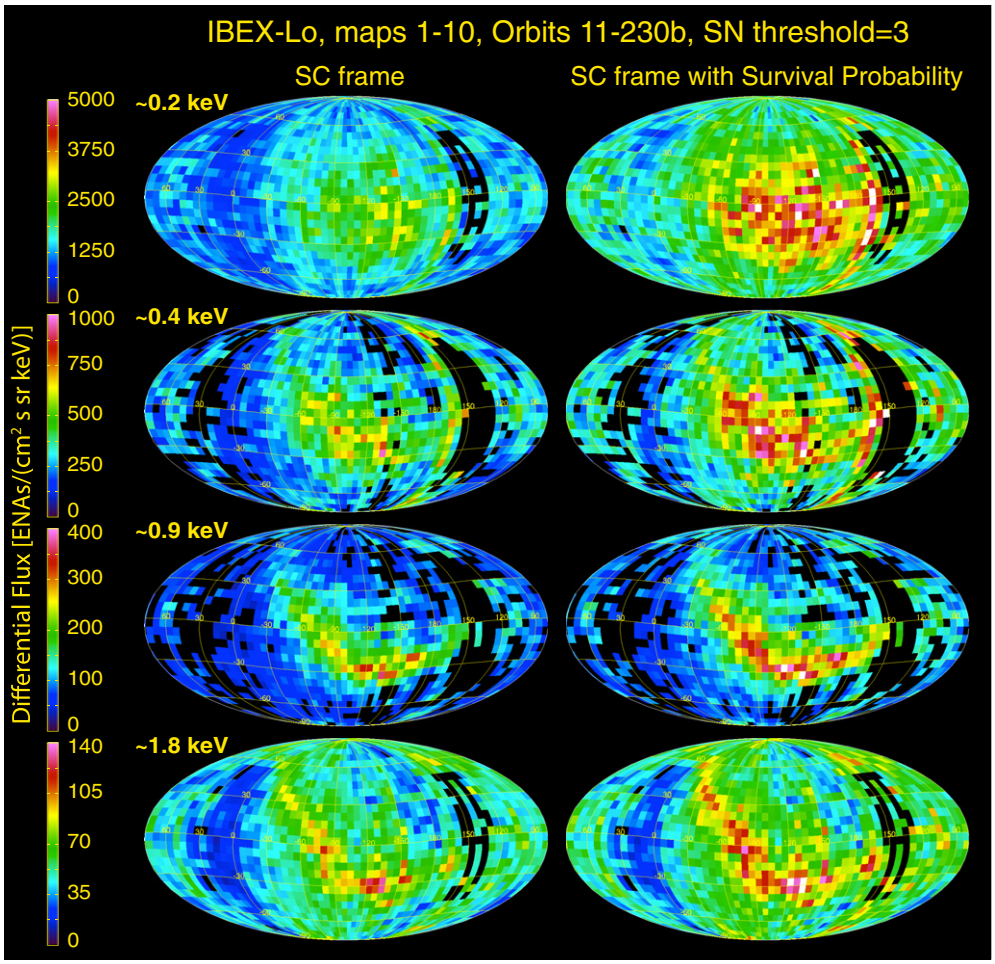

Figure 14. New *IBEX*-Lo maps, combining five years of observations in the spacecraft frame—uncorrected (left) and corrected for survival probability (right). From top to bottom, the energy pass bands are centered around 0.2, 0.4, 0.8, and 1.8 keV. Pixels with a signal to noise ratio <3 have been suppressed (black).
(A color version of this figure is available in the online journal.)

energy ENAs making it into 1 AU, and (3) focus on the annual ram and anti-ram maps separately, where each pixel represents the same energy and angle of ENA observations from one year to the next.

Figure 20 provides difference images for the ram maps at various energies. In each, Columns 2–5 show the percentage difference in fluxes between 2009 and years 2010–2013, respectively, compared to the 2009 fluxes. Overall, the figure shows a progressive reduction of flux over the five years being compared, with increasing fractions of the pixels becoming more and brighter blue (larger reductions), with time. The fact that the Ribbon is not an obvious feature in these all sky difference maps would suggest that the overall reductions in Ribbon flux have been generally similar to the reductions from the globally distributed flux from the surrounding regions of the sky, however, we take this issue up with more detailed analysis below. Finally, in the last year of observations (2013), the maps at the two highest energies show a marked asymmetry, with continuing and larger flux reductions in the northern hemisphere than in the southern one.

Figure 21 similarly shows flux difference images, but for the anti-ram maps. The features here are generally similar to those in Figure 20, but due to the poorer statistics because of lower fluxes at lower energies, we do not recommend these comparisons be used quantitatively. Furthermore, residual backgrounds have larger effects in anti-ram maps, which are even further exacerbated by the subtraction of fluxes to produce this figure. Thus, the results in Figure 21 should only be used as a guide to generally confirm the findings in the ram map comparisons (Figure 20).

Similar to what was done in the three-year paper, we further quantify time variations in survival probability-corrected ENA fluxes over several large regions of the sky. In this study, however, we have included an additional region covering the port and starboard slow wind lobes of the heliotail (McComas et al. 2013b). Figure 22 shows the four regions examined: (1) Ribbon, (2) nose and northern upwind side, (3) south polar region (plus flank below Ribbon), and (4) slow wind portions of the heliotail.

Figure 23 shows the integrated total ENA flux (corrected for survival probability) as a fraction relative to 2009 integrated fluxes for each of the four regions in Figure 22, and for the whole sky. Table 4 gives the quantitative changes from 2009 to 2013. In both, we note that error bars (often so small that they are hidden by the points) represent statistical errors and some small systematic errors related to background subtractions. For this analysis we excluded pixels with a zero in either of the years being compared and culled a few additional pixels where the variance was larger than the pixel's flux value.

One major result from the quantitative assessment of time variations is that except for the heliotail, the rest of the ENA fluxes have more or less leveled off in 2013 after dropping

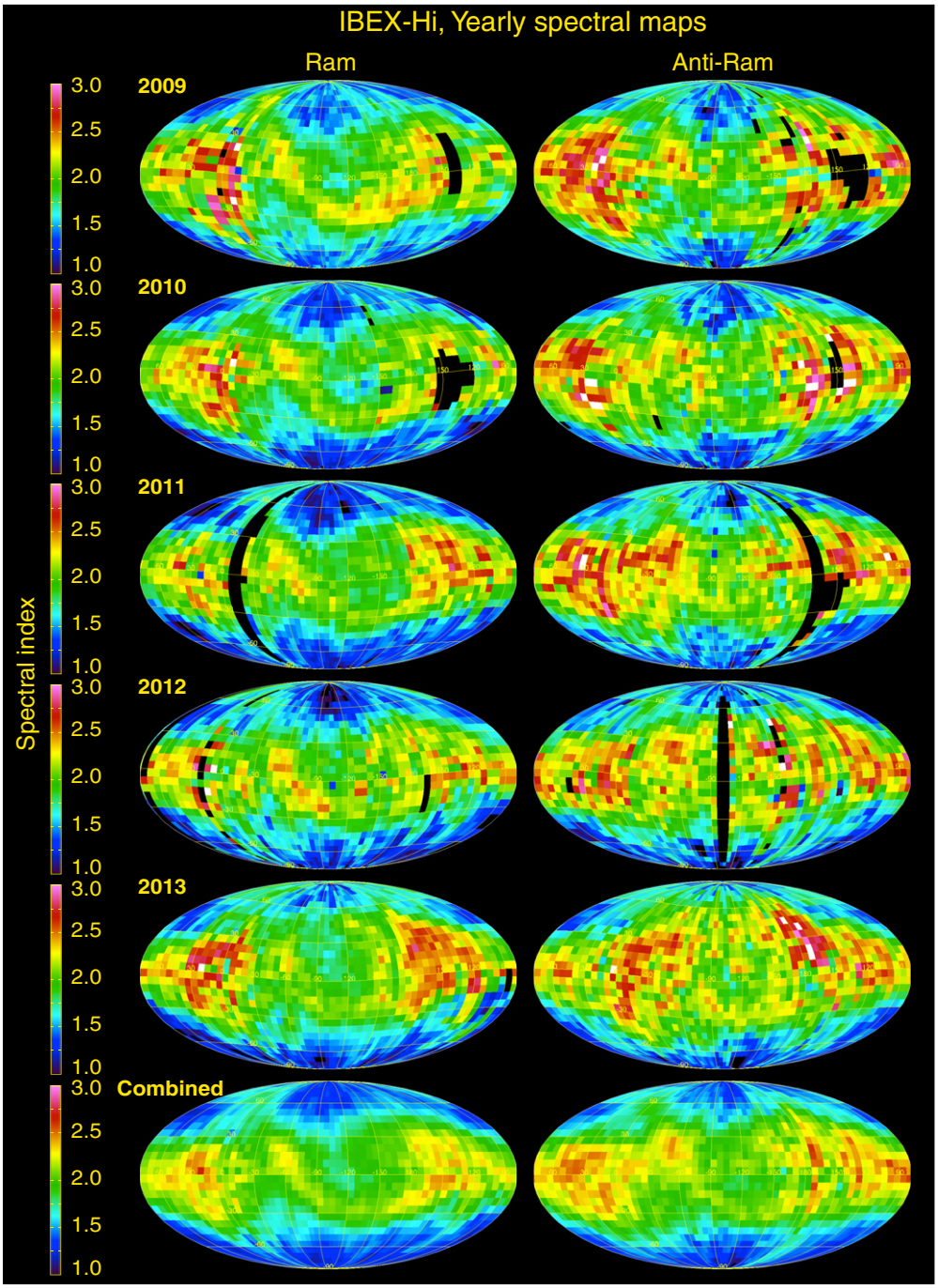

Figure 15. Sky maps of energy spectral index from ~0.5 to 6 keV in annual ram (left) and anti-ram (right) data for years 2009–2013 and all years combined (bottom). Energies are corrected to the solar frame (see the text).

(A color version of this figure is available in the online journal.)

Table 4
Quantitative Comparison of ENA Fluxes Between 2009 and 2013 in the Survival Probability Corrected Ram Maps; Errors Calculated as the Propagated Errors of the Weighted Flux Ratios Between the Compared Regions

Energy	Ratio of Weighted Fluxes in Annual SC Ram Maps ($Flux_{2013}/Flux_{2009}$)				
(keV)	(1) Ribbon	(2) Nose/N pole	(3) S pole/flank	(4) Heliotail	All Sky
~0.7	0.87 ± 0.01	1.02 ± 0.03	0.85 ± 0.02	0.7 ± 0.02	0.86 ± 0.01
~1.1	0.63 ± 0.01	0.72 ± 0.01	0.67 ± 0.01	0.71 ± 0.03	0.68 ± <0.01
~1.7	0.75 ± 0.01	0.66 ± 0.01	0.68 ± 0.01	0.66 ± 0.03	0.69 ± <0.01
~2.7	0.73 ± <0.01	0.64 ± 0.01	0.73 ± 0.01	0.64 ± 0.03	0.7 ± <0.01
~4.3	0.65 ± <0.01	0.64 ± 0.01	0.79 ± 0.01	0.62 ± 0.02	0.69 ± <0.01

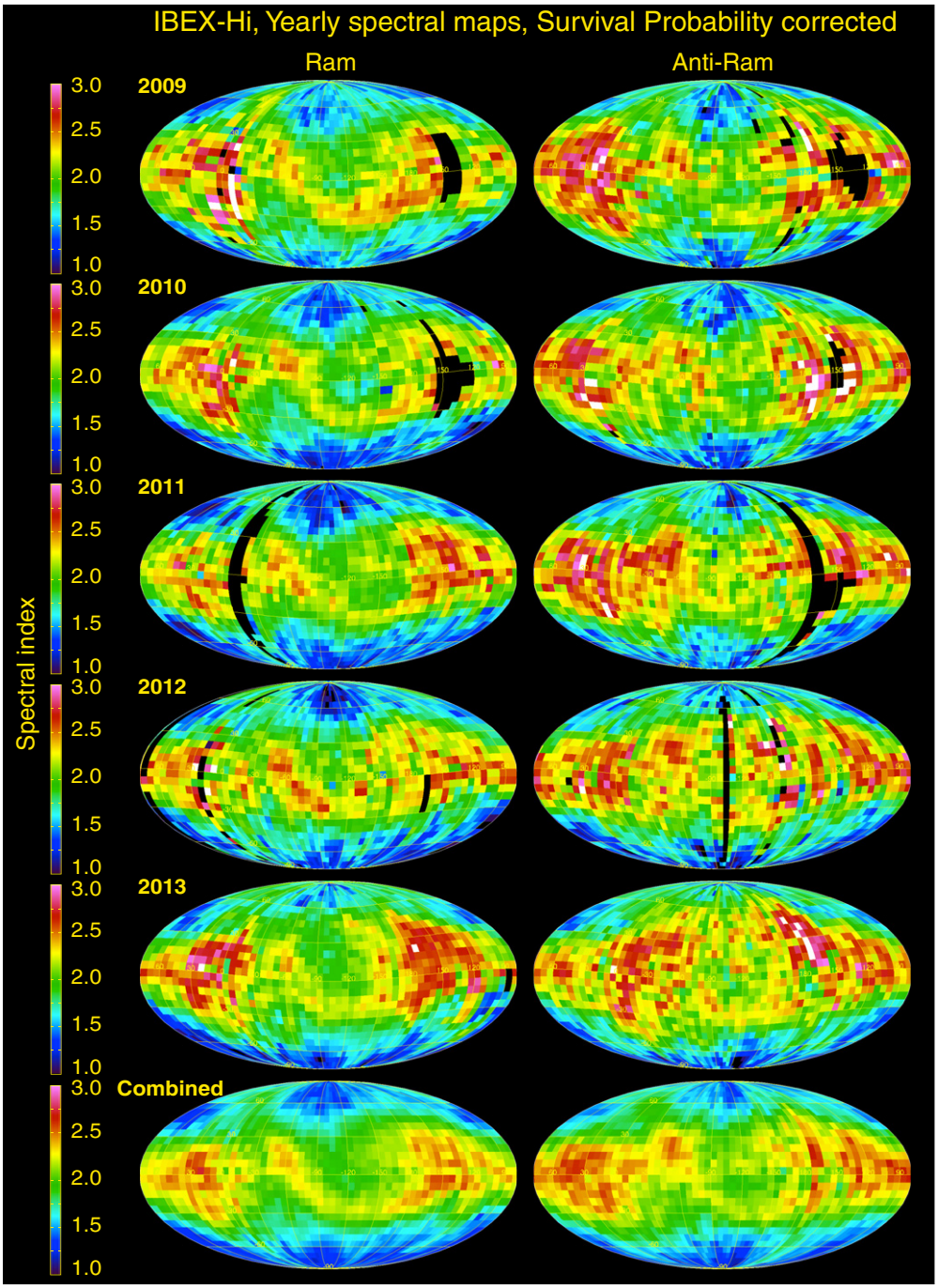

Figure 16. Same as for Figure 15, but survival probability corrected.
(A color version of this figure is available in the online journal.)

significantly from 2009 through 2012. This result is consistent with a simple predictive model of the likely ENA emissions in our prior three-year study (McComas et al. 2012b). That study used the solar wind properties averaged over a two year period from 2 to 4 yr before the central times of each *IBEX* map based on the simple arguments that for both the ~1 keV solar wind ions going outwards and returning ENAs at the same energy it takes about a year to travel the ~100 AU distance each way, and that the shocked solar wind plasma in the inner heliosheath effectively produces ENAs over ~2 yr. That simple model also used OMNI data as a proxy for the solar wind at all heliolatitudes; this is appropriately correct because, as shown by McComas et al. (2008, 2013a), the solar wind mass and momentum fluxes vary globally, so the ecliptic values of these two parameters (as opposed to speed and density separately, for example) are reasonably representative of all solar latitudes.

Using the above assumptions and simplifications, McComas et al. (2012b) predicted an overall leveling off in the fluxes from 2012 and 2013 to values ~0.8, 0.7, and 0.6 of the 2009 fluxes, depending on whether the mass flux, momentum flux, or energy flux (respectively) dominated the outer heliospheric interaction and generation of ENAs in the inner heliosheath (assumed for the 2–4 year time lag). The subsequent observations provided in this study do show a leveling off at ~0.7 (actually 0.72)

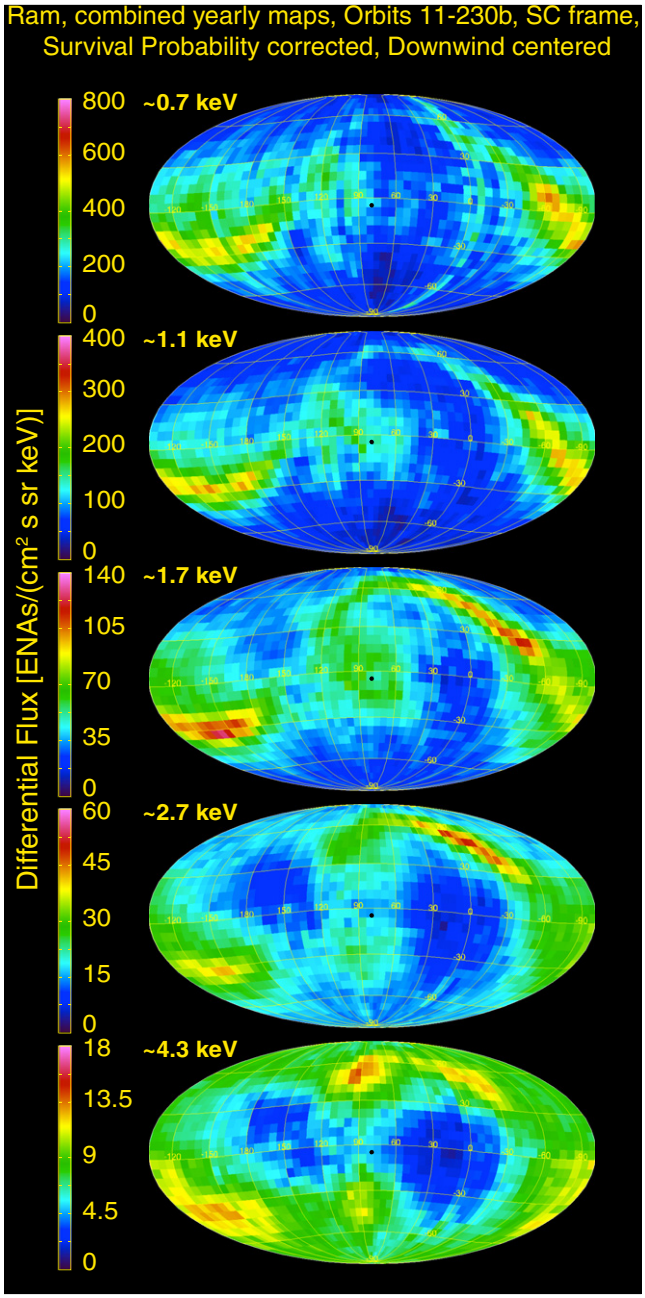

Figure 17. Centered on the downwind direction (opposite from standard Mollweide projections in prior figures).

(A color version of this figure is available in the online journal.)

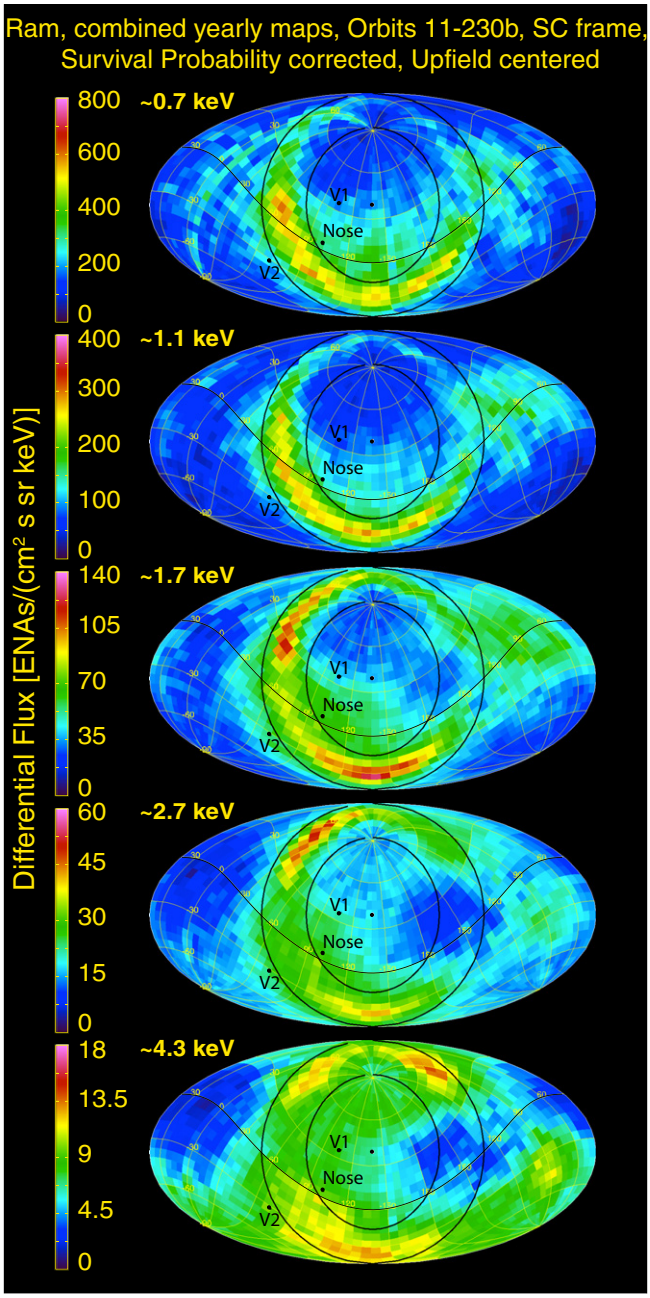

Figure 18. Mollweide projection of the five-year combined IBEX-Hi ENA fluxes centered on the upfield direction of the interstellar magnetic field. The circle and lines at the far left and right sides (same in all panels) roughly bound the Ribbon while the other curve across the maps indicates the ecliptic plane.

(A color version of this figure is available in the online journal.)

of the 2009 fluxes integrated over the entire sky for both Map 7 compared to Map 1 and Map 9 compared to Map 1, consistent with the predicted dominance of the momentum flux or dynamic pressure (ρv^2) of the solar wind. This association should not be surprising, as the dynamic pressure inflates the heliosphere, setting its overall size through pressure balance throughout the inner heliosheath and beyond, with the interstellar medium.

In contrast to the rest of the sky, the ENA fluxes from the slow wind lobes of the heliotail region (low to mid latitudes) continued to drop slightly in 2012–2013, reaching unprecedented levels of ~0.6 of the 2009 fluxes. This result is consistent with the emissions from the heliotail coming from significantly further away on average than on the noseward hemisphere or terminator (flanks and poles; McComas et al. 2013b). These emissions should represent a time lag from the slow, low to mid latitude solar wind at least a couple years longer than the assumed 2–4 yr, and thus still reflect the older, diminishing solar wind output (McComas et al. 2008, 2013a). As a new prediction, we would expect a leveling off in these fluxes from the slow solar wind heliotail lobes a couple years later than for the rest of the sky, so that can be tested in the upcoming several years of *IBEX* data.

For completeness, Figures 24 and 25 provide difference maps of the spectral slope for the uncorrected and survival probability corrected ram and anti-ram maps, respectively. These maps show significant pixel-to-pixel variability driven by flux variations and residual backgrounds to which the derived

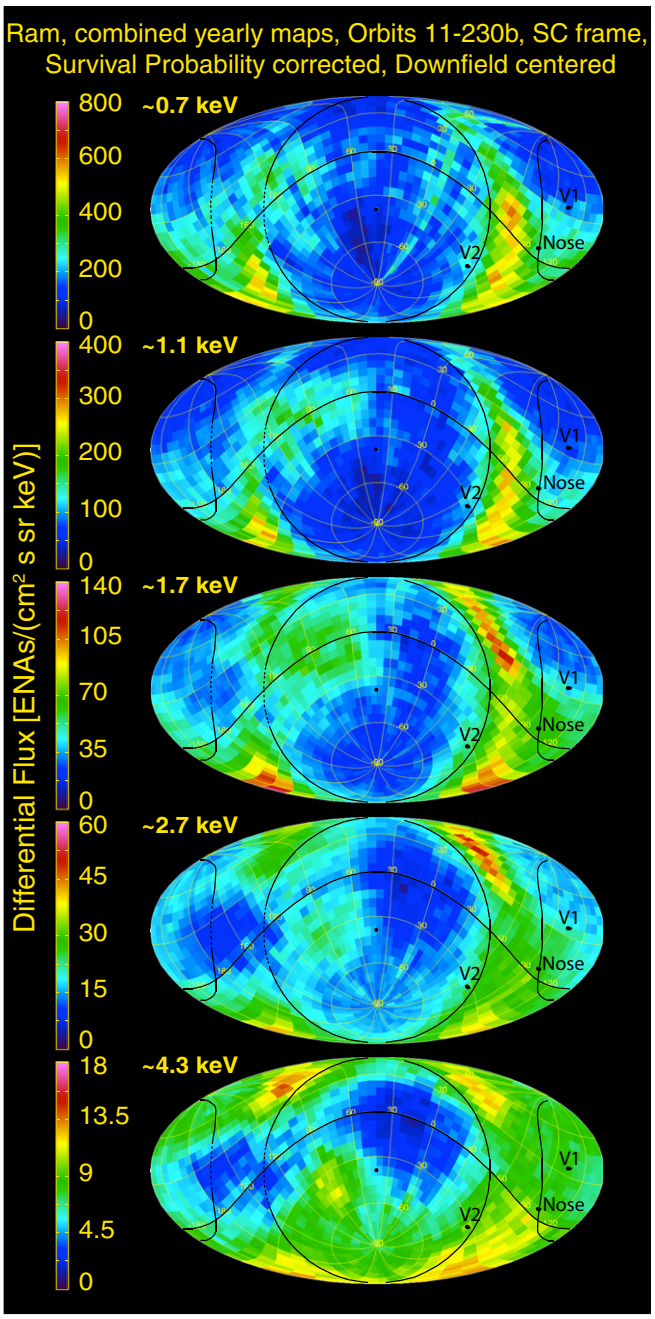

Figure 19. Similar to Figure 18, but centered on the opposite, downfield direction of the interstellar magnetic field. The lines again indicate the ecliptic plane and approximate boundary of the ribbon.

(A color version of this figure is available in the online journal.)

slope is very sensitive. Still, there is clearly an increasing spectral slope (red) in the upwind (towards the nose) hemisphere and decreasing spectral slope (blue) on the downwind side. The observed asymmetry suggests that the lower energy ENAs are decreasing more slowly than at higher energies on the upwind side and more than the higher energies on the downwind side. As for a similar effect seen in the just the north and south polar pixels (Allegrini et al. 2012), such an asymmetry is likely caused by the greater distance for the solar wind ions to travel and ENAs to return from on the downwind side compared to the upwind and the generally decreasing solar wind output. Figures 24 and 25 also show a substantial north–south asymmetry developing on the upwind side, especially in the 2013 maps (right columns), with broadly increasing spectral slope in the north, but not in the south.

Because of the statistical variability, individual pixels in the time variation sky maps (Figures 20 and 21) can show very large pixel-to-pixel variations, which make it hard to discern true variations. Thus, in Figure 26, we statistically combine pairs of survival probability corrected ram maps from 2009/2010 and 2012/2013, and calculate percentage changes between these new composite maps. Differences represent changes over the three years average time separation between the two sets of maps. The improved statistical significance is obvious, with much smoother spatial variations in the percentage difference maps. The Ribbon is a discernible feature with greater reductions in the 0.7 and 1.1 keV maps and lesser reductions in the 1.7 and 2.7 keV maps (at least in the horizontal portions), thanks to the surrounding globally distributed flux.

Because the Ribbon emissions at different energies are clearly latitude dependent, and in order to try and reduce the effects of the superposed globally distributed flux, which has clearly leveled off over 2012–2013, in Figure 27, we single out latitude ranges based on areas of enhanced fluxes in the Ribbon at various energies. In addition, we exclude overlapping emissions from the slow solar wind lobes of the heliotail. Focusing on these much more specific emission regions, we reanalyze the time history of ENA emissions from the Ribbon in Figure 28.

Figure 28 shows the time evolution of ENAs for the dominant energy/latitude dependent emission regions of the Ribbon. From 2009 to 2012, ENA fluxes are declining at all energies in both the northern and southern portions of the Ribbon. However, in 2013, while the northern Ribbon ENAs continue to show declining fluxes, especially for the highest two energies, the southern Ribbon ENA fluxes appear to have flattened out or even slightly recovered. Thus, the evolution of the Ribbon fluxes in the two hemispheres has become quite different in 2013. We note that this difference cannot be simply explained by the difference in the survival probability corrections, which diverge between the north and south in 2012–2013 (e.g., Figure 6) as these corrections are only a few percent different, especially at the higher energies were the Ribbon flux evolution becomes so different.

Perhaps this divergence can be explained by significant differences in the distance to the Ribbon source regions in the north and south, especially at higher latitudes/energies. The southern portion of the Ribbon is almost certainly closer to the Sun than the northern portion for several reasons: (1) the Ribbon does not extend to as high latitudes in the south as in the north, (2) the southern portions of the Ribbon are largely on the upwind, and thus compressed, side of the heliosphere, while the northern portions wrap back around the north pole on its downwind side, and (3) the heliosphere is compressed in the south compared to the north, owing to the inclination of the strong external field surrounding the heliosphere (McComas et al. 2009c; Schwadron et al. 2009; Opher et al. 2009).

4. DISCUSSION

IBEX's all-sky ENA observations have provided an incredible window into the global nature of the outer heliosphere and its interaction with the surrounding, very LISM. These results have included the first observations of globally distributed fluxes of ENAs from the inner heliosheath and the discovery of the Ribbon and heliotail. Latitudinal ordering of the fluxes as a function of ENA energy reflects the solar wind's bimodal

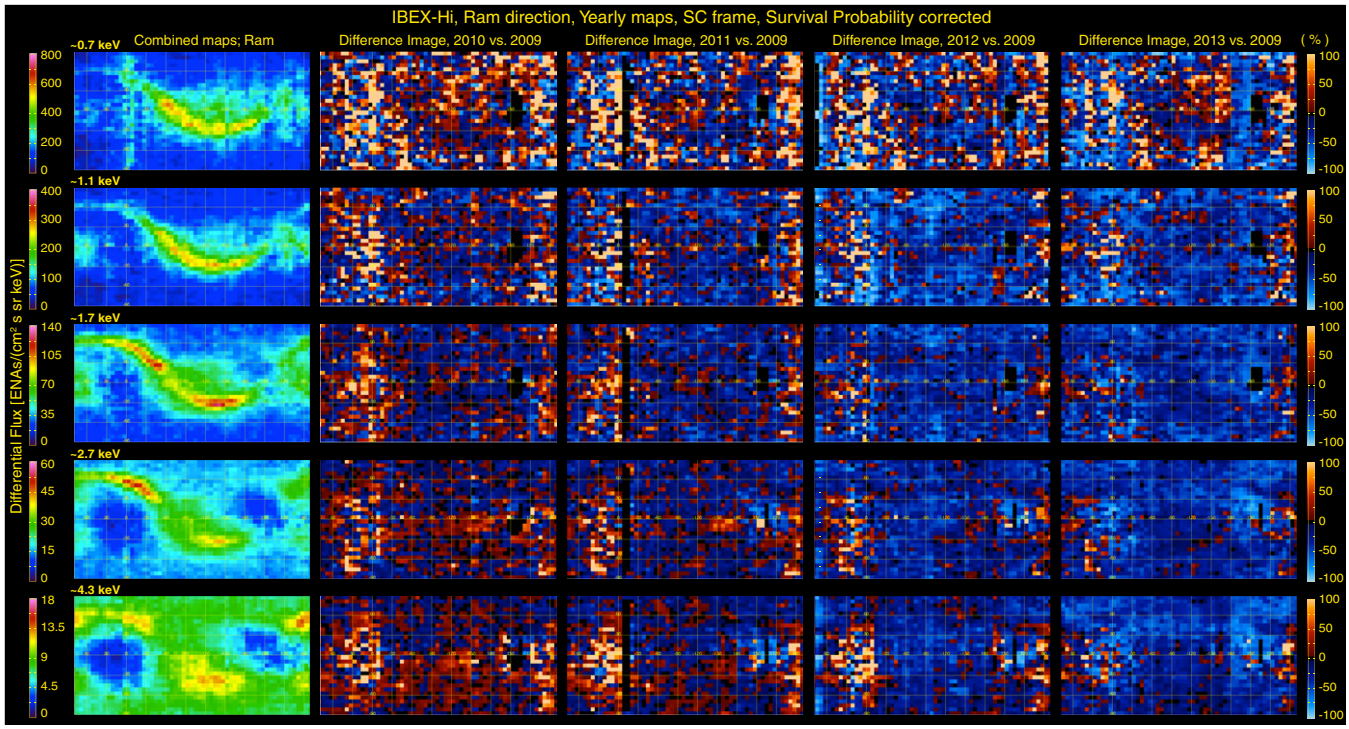

Figure 20. Time variations in survival probability corrected ram maps comparing ENA fluxes from 2010 to 2013 with 2009 (Columns 2–5, respectively). The left column shows the average ENA fluxes over the five years as a guide. For each pixel, the percentage change is calculated as 100× the new value minus the 2009 value divided by the 2009 value.

(A color version of this figure is available in the online journal.)

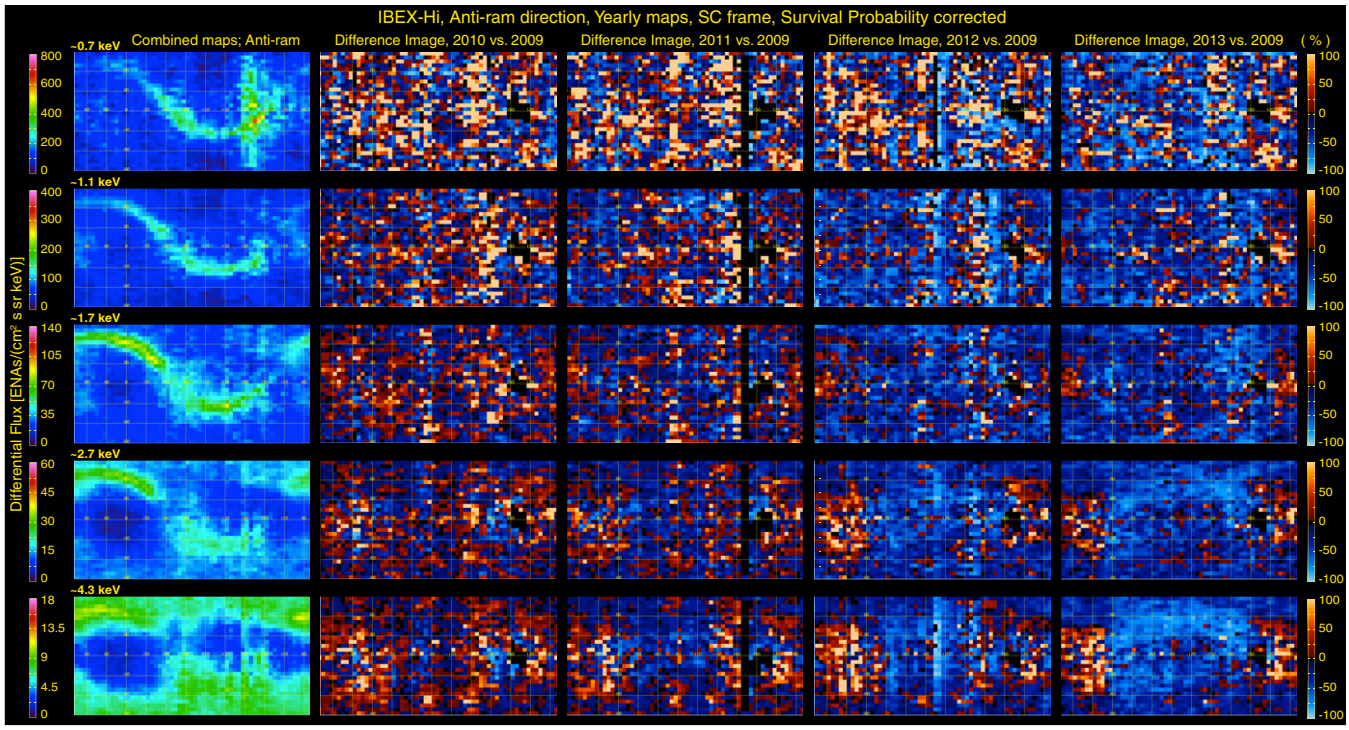

Figure 21. Similar to Figure 20, but for anti-ram maps from 2010–2013 compared to 2009.

(A color version of this figure is available in the online journal.)

latitudinal structure around solar minimum in all three of these source regions, although the detailed processes may be different.

IBEX observations have demonstrated the truly critical roles that the interstellar magnetic field plays in shaping and driving the physical processes of the outer heliosphere. These include the orientation of the ribbon, asymmetric compression of the heliopause, and even tilting/twisting of the heliotail structure. *IBEX* results have also shown the key role that charge exchange plays in the outer heliosphere—coupling the plasmas across spatial scales of hundreds of AU and boundaries that are

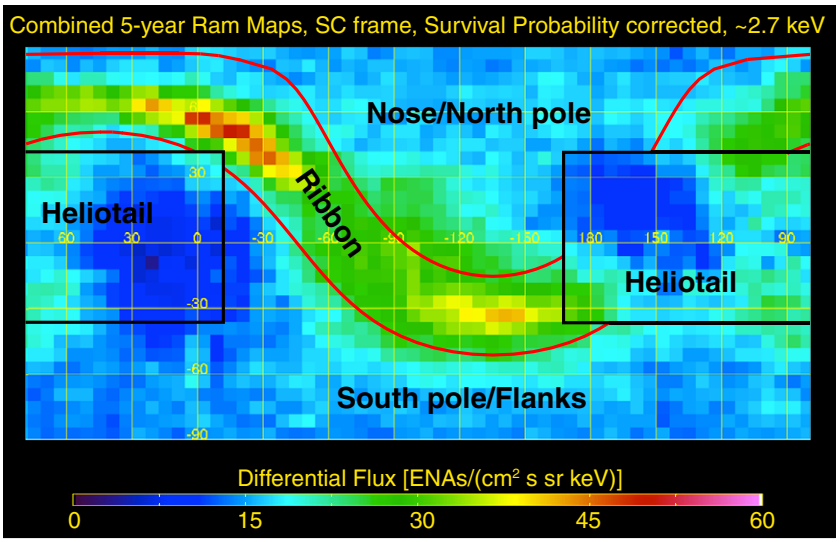

Figure 22. Combined 5 year ram map at 2.7 keV overlaid with lines identifying broad regions in the sky maps integrated for numerical comparison of the time variations.

(A color version of this figure is available in the online journal.)

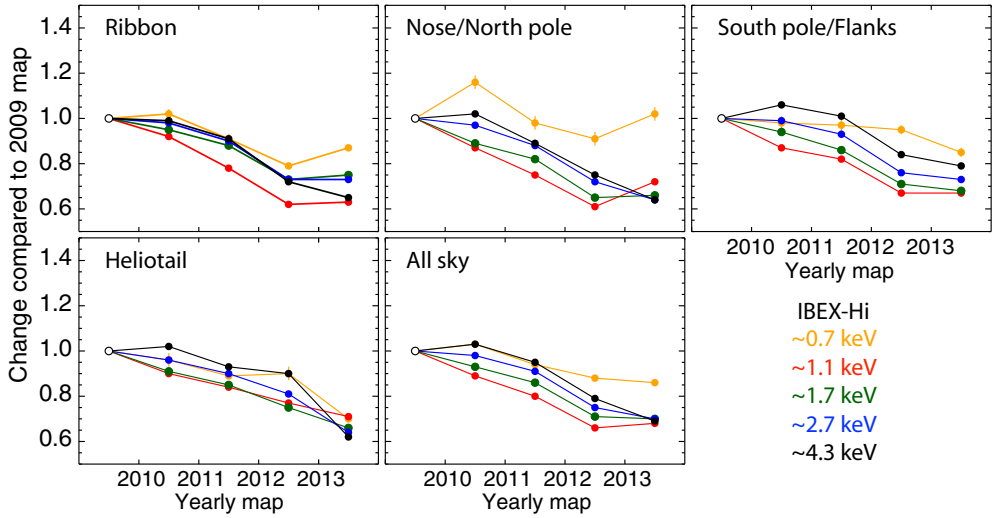

Figure 23. Time variation of ENA fluxes over broad regions and for the whole sky (see Figure 22). Energy pass bands are identified by color and plotted along with statistical error bars (smaller than the dots in many cases), normalized to the 2009 fluxes.

(A color version of this figure is available in the online journal.)

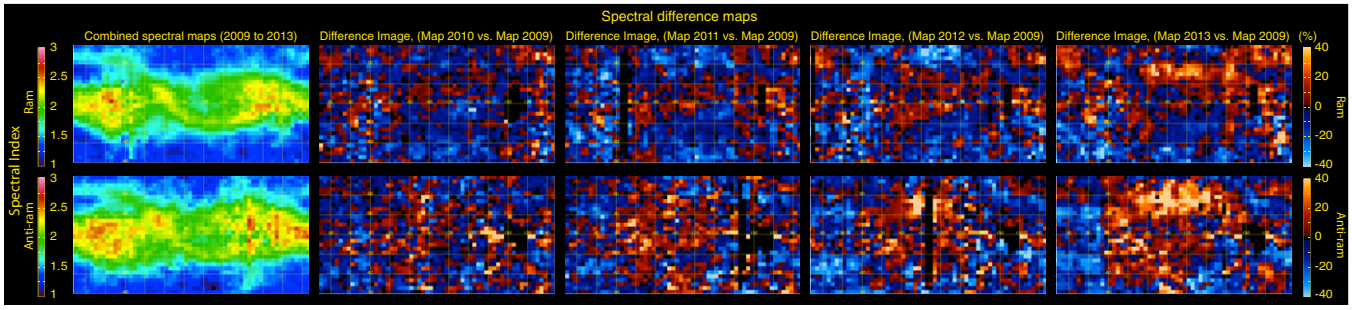

Figure 24. Spectral indices for the five year combined ram (top) and anti-ram (bottom) maps (left column). Columns 2–5 show the percentage change in these indices for 2010–2013, compared to 2009, respectively. As in Figures 20 and 21, for each pixel, the percentage change is calculated as 100× the new value minus the old value divided by the old value.

(A color version of this figure is available in the online journal.)

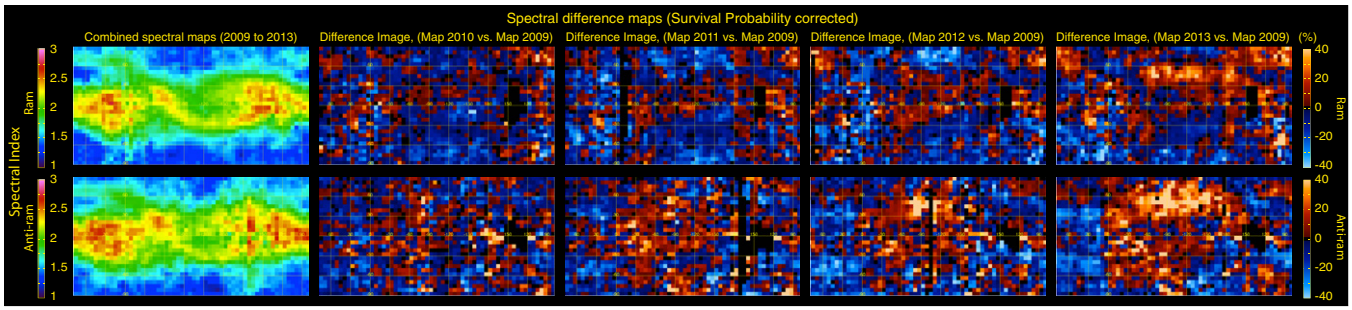

Figure 25. Similar to Figure 24, but including survival probabilities.
(A color version of this figure is available in the online journal.)

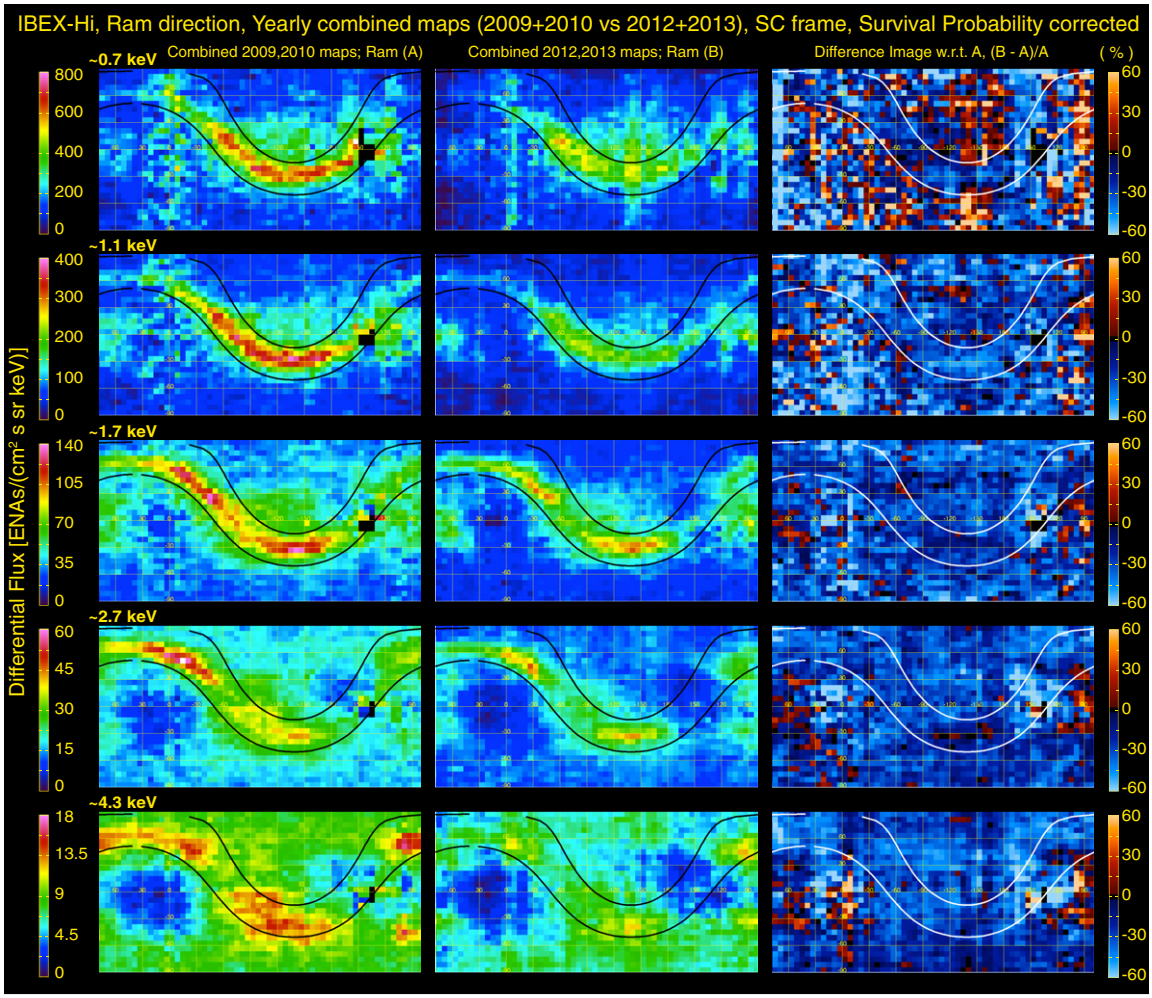

Figure 26. Combined survival probability corrected Ram maps for 2009+2010 (left column), 2012+2013 (middle), and the percentage difference between the two sets of maps.
(A color version of this figure is available in the online journal.)

fundamentally changed by the ion-neutral coupled behavior, as for example the bow wave (no longer thought to be a bow shock based on *IBEX* observations; McComas et al. 2012a) and hydrogen wall (e.g., Zank et al. 2013).

ENA temporal variations, with reductions in the ENA fluxes from 2009 through 2012 and a leveling off in 2013, are consistent with predictions made by McComas et al. (2012b) based on the overall solar wind output 2–4 yr earlier, which is a reasonable "recycle" time for solar wind to reach the termination shock, travel in the inner heliosheath for a while, and return as ENAs. Figure 29 shows this general connection between the solar wind from several years earlier and observed ENA fluxes for 2009–2013. Based on the same simple thinking, here we predict that the all-sky ENA fluxes for 2014 and 2015 should continue to be largely flat or increase slightly, but not back up to their 2009 levels. For the heliotail, the recycle time should be years longer and thus fluxes from this region have continued to drop in 2013, in contrast to the rest of the sky, and should only flatten out after a couple more years. Finally, the Ribbon emission time history is more complicated, showing a leveling off near the nose and in the south, but continued reductions at higher northern latitudes, again consistent with a great distance to the source of the Ribbon

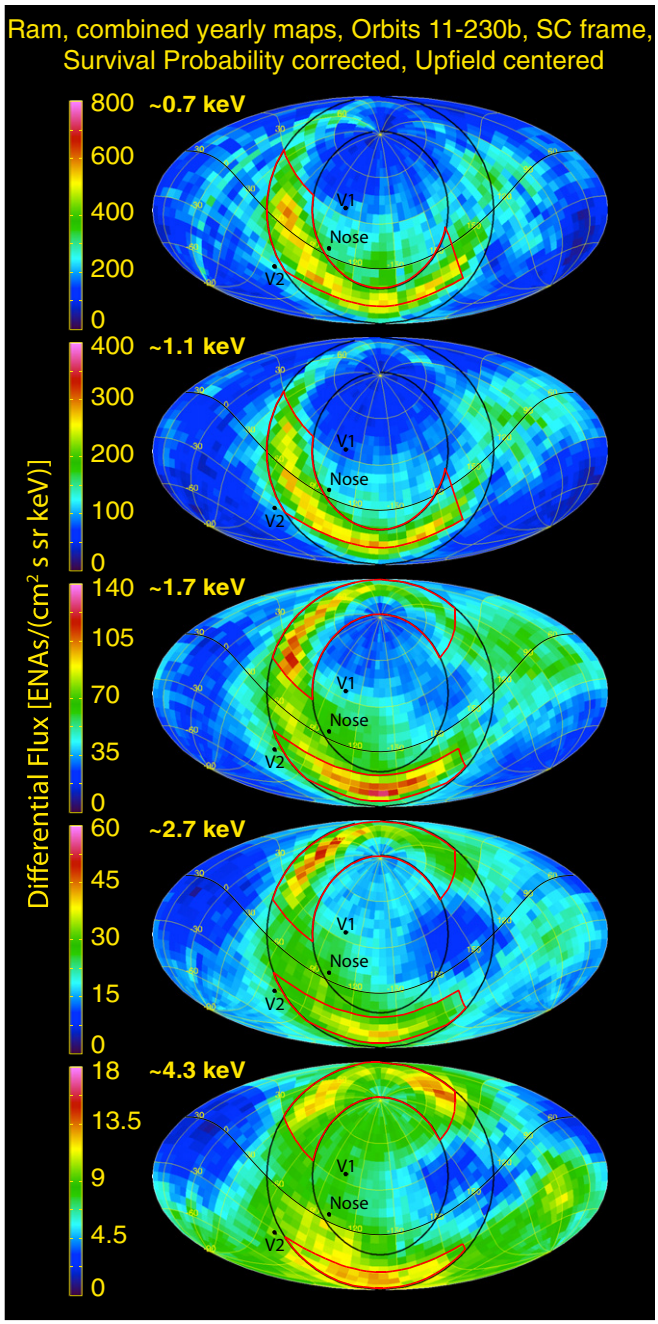

Figure 27. Selection of dominant Ribbon ENA emission regions (red outlined areas in each map). Ribbon emissions are strongest at increasingly higher latitudes for higher energies, consistent with the latitude ordering of the solar wind around solar minimum (McComas et al. 2012b). Specifically, these regions are ESA 2 and 3 North 0° to 30°, South −30° to 0°; ESA 4 and 5 North >18°, South −42° to −18°; ESA 6 North >30°, South <−30°; all regions further exclude the heliotail slow solar wind lobes.

(A color version of this figure is available in the online journal.)

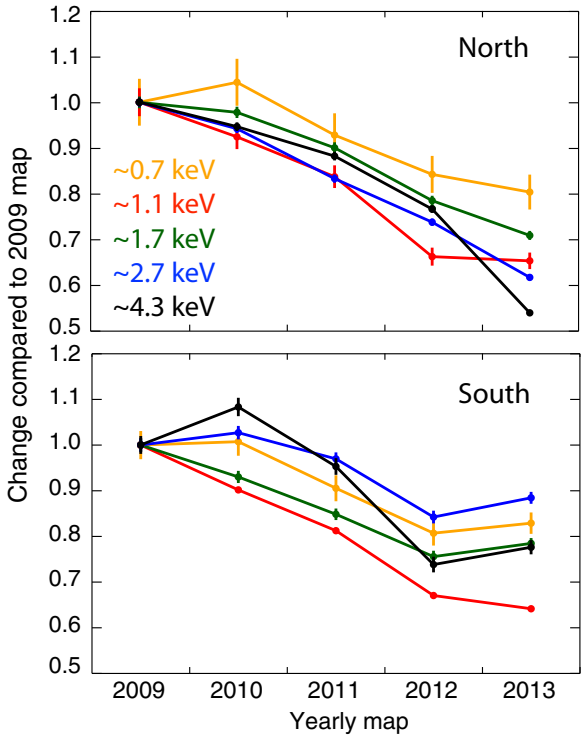

Figure 28. ENA fluxes at various energies from the latitude-dependent Ribbon regions specified in Figure 27. The northern hemisphere (top) and southern hemisphere (bottom) fluxes show similar reductions from 2019 to 2012, but clearly diverge in 2013.

(A color version of this figure is available in the online journal.)

around the high latitude flanks on the downwind side of the north pole.

Globally, there is evidence in the 2013 data of a developing asymmetry between the northern and southern hemispheres at the highest two ENA energies, especially on the upwind (nose) side, with a leveling off in the southern hemisphere and continued (though smaller) reductions in the south. As pointed out above, this could be consistent with a greater distance to the inner heliosheath emission regions in the north than in the south. The Ribbon also shows a quite different behavior in 2013 with the northern Ribbon ENA flux continuing to drop and southern flux leveling off. While consistent with an inner heliosheath source at greater distances in the north, this variation is also consistent with a secondary ENA source mechanism for the Ribbon (e.g., McComas et al. 2009c; Chalov et al. 2010; Heerikhuisen et al. 2010; Schwadron & McComas 2013). A secondary ENA source is further out, past the heliopause in the outer heliosheath. For such a configuration, the greater distance to the Ribbon's northern portions than its southern ones could easily account for a longer time lag and an older solar wind source being observed in the north and thus the continued reductions in the ENA fluxes.

One issue with the time variation of the observed ENA fluxes from both the Ribbon and globally distributed flux is that changes do not generally seem to begin with the highest energies and then progress smoothly to lower and lower energies. This time dispersion is what one would naively expect for a temporally changing source at a fixed distance simply owing to the fact that higher energy ENAs propagate faster than lower energy ones and thus could provide earlier evidence of a change, such as a leveling off of the flux. However, a secondary ENA Ribbon source might not show this expected time dispersion. As pointed out by Möbius et al. (2013) the energy dependent charge exchange cross section should cause the Ribbon source region for secondary ENAs to be farther away for higher energies compared to lower energies. This could compensate for the faster speed of higher energy ENAs and allow the change in slope or even turn up to appear to occur simultaneously as opposed to showing time dispersion for different energies.

The outer heliosphere is also a very complicated and dynamic environment with the energies of the source solar wind as

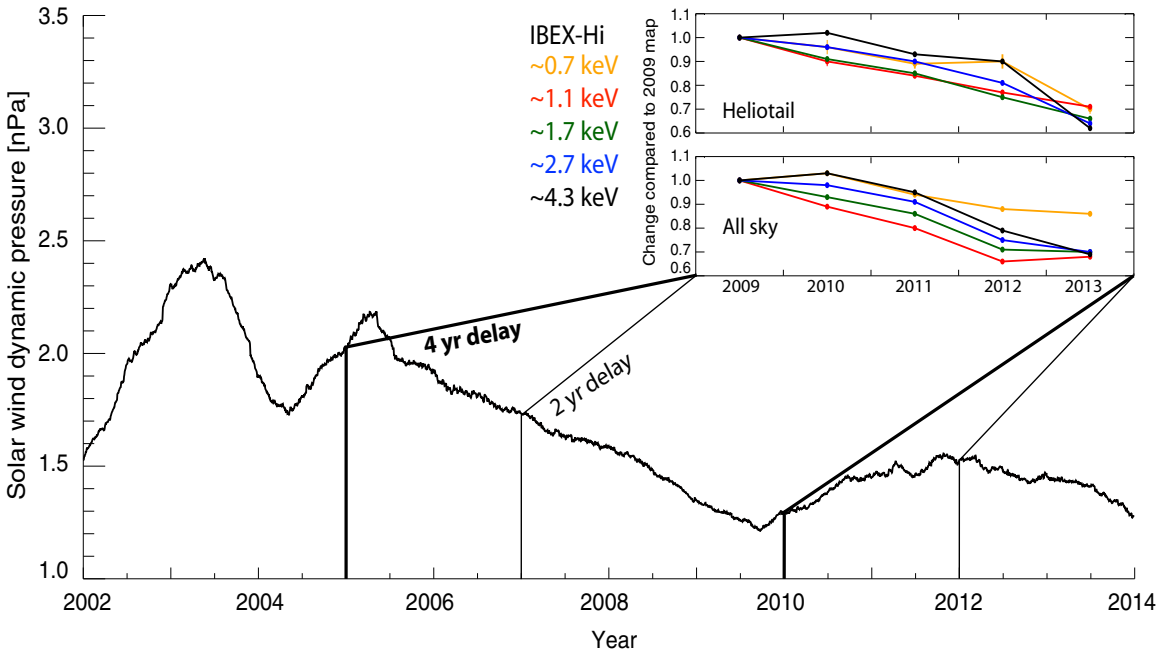

Figure 29. Solar wind dynamic pressure (one year smoothing, bottom) and ENA fluxes measured by *IBEX*, relative to their 2009 values for both the entire sky and for the slow wind lobes of the heliotail only (McComas et al. 2013b).

(A color version of this figure is available in the online journal.)

well as the flux playing important roles. For a slowing solar wind, as has been seen over most of the time relevant to *IBEX* (McComas et al. 2013a), the source population should shift from higher to lower energies, decreasing the fluxes of the former and increasing the fluxes of the latter. In addition, the outer heliosphere is constantly trying to adjust to a state of pressure balance between the ever-changing solar wind and external pressure from the interstellar medium. This evolving balance compresses and can heat and cool the plasma locally, also leading to shifts in the energy spectrum of the resultant ENAs. Finally, as examined recently in a theoretical study by Siewert et al. (2013), losses from the charge exchange of ions in the outer heliosphere play a fundamental role in determining the remaining ion populations and produce very complicated sources for the observed ENAs; these sources favor emission regions closer in to the termination shock and are strongly driven by look direction and energy as well as the time variable solar wind. In the end, the situation is so complex that global 3D models may be the only way to quantitatively link the evolution of the solar wind source and observed ENA fluxes.

The downwind and downfield centered perspective shown in Figures 17 and 19, respectively, are interesting ones for assessing the relative importance of ribbon versus tail emissions at the locations where the circular structure of the Ribbon would cross the heliotail. From this perspective, it seems clear that the tail structure dominates across the downwind side and the Ribbon; the Ribbon is continuous elsewhere (at the appropriate latitude dependent energies), but appears largely absent through the tail. This observation may provide an important differentiation between the various Ribbon models (see McComas et al. 2014, and references therein). If the Ribbon were produced by ENA emissions from the inner heliosheath, as many of the source ideas suggest, then there is no a priori reason that similar emissions would not also arise from the nearby tailward portions of the inner heliosheath in fluxes similar to those elsewhere in the Ribbon. On the other hand, for any of the secondary ENA emission scenarios, the source is in the outer heliosheath, much farther away on the downwind side. Losses of ENAs created at such large distances (many hundreds to thousands of AU) are so great that they would likely make any residual Ribbon very faint if observable at all (Möbius et al. 2013); we note that there is at least the possibility of a faint ribbon across at least part of the downwind side.

McComas et al. (2012b) made a prediction that applies to any secondary ENA sources of the Ribbon. That is, once solar wind from solar maximum, when the speeds are no longer ordered by solar latitude (e.g., McComas et al. 2003), are returned to 1 AU as ENAs, the latitudinal ordering of the ENA energies in the Ribbon should similarly disappear. Instead, the Ribbon should comprise low-to-intermediate energy ENAs at all solar latitudes as fast and slow solar wind flows interact at all heliolatitudes around solar maximum. The *IBEX* results through 2013 clearly still show the latitude-energy ordering indicative of the global solar minimum solar wind, as expected. The Sun has now past solar maximum, which was the smallest solar maximum of the space age, with the smallest solar wind output (McComas et al. 2013a). However, it should still be several more years before secondary ENAs from maximum return.

5. THE FUTURE OF OUTER HELIOSPHERIC RESEARCH

The *IBEX* mission has already yielded an incredible harvest of first observations and new discoveries about the outer heliosphere and its interaction with the LISM (e.g., see Table 1). Five years ago, no one even knew about the existence of the Ribbon of enhanced ENAs streaming in from the outer heliosphere, and no models predicted, or even anticipated, its existence. Worse yet, similarities between some aspects of the *Voyager 1* and *2* observations were taken as prima facie evidence that the interaction varied little between their vastly separated locations. Today, we know that the outer heliosphere is a far more complicated, structured, and variable region—and far

more interesting. However, we still do not even know the origin of the Ribbon (see McComas et al. 2014), and we are just beginning to see how the variable solar wind structure modifies and dictates the global ENA emissions.

With the combined in situ measurements of the two *Voyagers* and global imaging provided by *IBEX*, the past five years have truly been a golden age of outer heliospheric research, science, and discovery. The heliosphere's interaction with the LISM is incredibly important for humanity as it provides shielding for the inner solar system from the vast majority of galactic cosmic rays. Such an interaction may even be a key enabling factor in the habitability of other stellar systems—just as liquid water is considered a likely key ingredient. Unfortunately, the *Voyager* spacecraft will not last forever. Current estimates based on RTG aging suggest that both *Voyager* spacecraft have adequate power for all instruments until ∼2020, and decreasing power for fewer and fewer instruments out to the end of mission sometime after ∼2025. In addition, while *IBEX* has already operated well over two and a half times it nominal mission lifetime, there is no way to know how long this very low cost, Small Explorer can continue to survive.

Thus, the heliophysics community needs to move forward quickly in implementing a follow-on Interstellar Mapping (IMAP) mission (e.g., McComas et al. 2011b), which has been recommended by the National Academy's Decadal Survey: *Solar and Space Physics: A Science for a Technological Society*; National Research Council 2013) as the next identified mid-sized Heliophysics mission. Such a mission would both extend the critical global imaging observations through the *Voyagers*' lifetimes and provide much higher sensitivity and spatial resolution as well as a longer, uninterrupted temporal baseline for a vastly better understanding of the heliosphere's interstellar interaction. It is only through the rapid development of a new IMAP mission that the heliophysics community can capitalize on the incredible opportunity that the *Voyagers* currently enable; without IMAP the nation and international science community will squander what is truly a once in a lifetime—even once in a century—opportunity.

We thank all of the outstanding men and women who have made the *IBEX* mission such a wonderful success. This work was carried out as a part of the *IBEX* project, with support from NASA's Explorer Program and Polish National Science Center grant 2012/06/M/ST9/00455. We also gratefully acknowledge the McMurdo data from the Bartol Research Institute neutron monitor program, which is supported by the United States National Science Foundation under grants ANT-0739620 and ANT-0838839, and by the University of Delaware Department of Physics and Astronomy and Bartol Research Institute. Work at Los Alamos was performed under the auspices of the US Department of Energy.

APPENDIX A

TIME VARIABLE COSMIC RAY BACKGROUND CORRECTION IN *IBEX*-Hi

IBEX-Hi data is subject to a variety of backgrounds. Some are always present to some degree; some are present only over limited times and at limited angles, such as foreground objects (e.g., Earth magnetosphere and the moon) and deflected solar wind contamination. Data intervals, in angle and time, are sorted into one of three categories: "good," "loose," and intervals not currently used for heliospheric science. In "good" periods, the data appears statistically consistent with the quietest intervals of an orbit arc and does not contain any additional intermittent signal. "Loose" periods have at most a small and (nearly) isotropic additional background beyond those in the good times. Loose intervals are selected infrequently, as the data permits, and are treated by the subtraction of a small offset for a presumed isotropic background (not scaled) to match on average the signal rate observed in the good cull intervals.

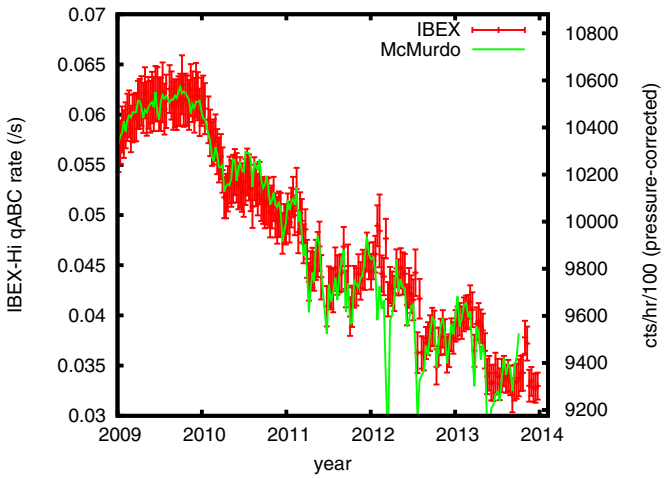

Figure 30. Penetrating background rate for qualified triples, calculated orbit by orbit excluding SEP events, compared to the McMurdo neutron monitor rates. (A color version of this figure is available in the online journal.)

Even in the "good" intervals, some always-present backgrounds remain. The principal such background is penetrating background due to cosmic radiation (another: the ion gun background is discussed in Appendix D). As in McComas et al. (2012b), penetrating background appears in the "qualified" triple-coincidence count rate, which is the cleanest *IBEX*-Hi data product and the one used in the five-year maps. However, the fraction of qualified triple coincidences, where the event is registered in detector section A (the "front" of the detector) prior to registration in detector section C (the "back"), is different between ions and penetrating background. Nearly all signal ions are detected in section A first, as shown during calibration (Funsten et al. 2009b), whereas only roughly half of penetrating radiation is detected in section A first. This ratio for penetrating background was measured in orbits 13, 77, and 189 (2009 January, 2010 May, and 2012 December) and has not changed over time. Penetrating background is then calculated from the number of qualified triples, the number of unqualified triples, and the predetermined ratios of the two for signal and background (Funsten et al. 2009a).

The penetrating background correction is calculated for each orbit's worth of data, and thus is approximated as constant over that interval. Times of solar energetic proton events are excluded from this determination as the *IBEX*-Hi data is generally culled out at such high background times. Uncertainty arises from the counting statistics; systematic uncertainty arises from the calibrated ratio of coincidence types for ENAs (determined in calibration) and for background (determined on-orbit).

Figure 30 shows a comparison of *IBEX*-Hi calculated penetrating background as a rate of qualified triples (red data points, vertical axis on the left), compared to the McMurdo neutron monitor data (green curve, vertical axis on the right) over the same interval. The error bars shown for *IBEX* include statistical uncertainty and systematic uncertainty arising from the

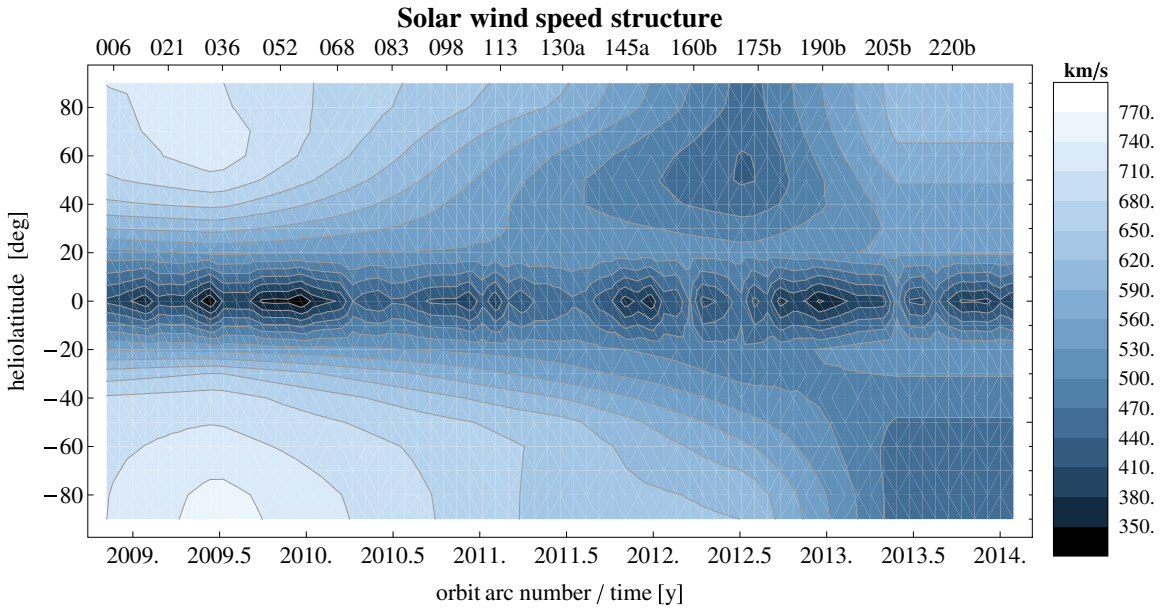

Figure 31. Solar wind speed evolution as a function of time and heliolatitude. The vertical axis is heliolatitude, the lower horizontal axis is time in calendar years, and the upper horizontal axis presents the corresponding intervals for *IBEX* orbital arcs.

(A color version of this figure is available in the online journal.)

uncertainty in the unqualified ABC to qualified ABC ratios for ENAs and for penetrating background. A scaling factor is needed to correlate the data types, and an offset is necessary due to the atmospheric low energy cutoff around 700 MeV for the McMurdo measurements. The scaling factors in this figure are identical to those used in McComas et al. (2012b), indicating the long-term stability of *IBEX*-Hi as well as understanding the causal factors for this background.

APPENDIX B

UPDATES ON SURVIVAL PROBABILITY CORRECTIONS FOR BOTH *IBEX*-Hi AND *IBEX*-Lo

The flux of heliospheric hydrogen ENAs is attenuated inside the termination shock due to ionization by charge exchange with solar wind protons, photoionization, and solar wind electron impact. Details on the construction and solar cycle behavior of the ionization rates were presented in a recent review by Bzowski et al. (2013). Survival probabilities of heliospheric ENAs were discussed by Bzowski (2008) and details of the survival probability calculations for the heliospheric ENAs observed by *IBEX*, as well as solar wind and solar EUV radiation data sets used, were presented in Appendix B in McComas et al. (2012b).

B.1. Updated Heliolatitudinal Structure of the Solar Wind Speed

The survival probabilities used in this paper are an update and extension of the survival probability system used by McComas et al. (2012b). The heliolatitude-dependent evolution of solar wind speed comes from the Computer Assisted Tomography of the interplanetary scintillations (IPS) observed by the Solar-Terrestrial Environment Laboratory at Nagoya University, Japan (Tokumaru et al. 2012), and the in-ecliptic variation is obtained from the OMNI-2 time series, compiled from in situ observations (King & Papitashvili 2005). The IPS data are released once per year, after the observations are completed before the yearly winter break (Tokumaru et al. 2012). The IPS observations provide Carrington maps of solar wind speed, which we process to obtain yearly averages (Sokół et al. 2013) and form the basis for our model of solar wind speed and density. The OMNI-2 data are released with approximately 1 month delay in a preliminary form, and the final time series is released some time later.

Because of this delay in data availability, McComas et al. (2012b) applied an extrapolation of the solar wind evolution model for the interval after the data were available. This was after middle of 2011, or Orbit 130. Starting from that orbit, those authors "froze" the 3D solar wind structure, but the in-ecliptic variation of solar wind and EUV radiation was continued through the later available data. As a result of this necessary procedure, the survival probabilities calculated for Map 6 were not fully accurate. In the present paper, they were recalculated based on solar wind heliolatitude data that became available since that time.

Again, because of the delay in data availability, we now extrapolate for the last map (Map 10) of this study. The freezing of the heliolatitudinal structure of the solar wind speed in this study starts from the end of May 2013 (Orbit 207b). The in-ecliptic time series was frozen after orbit 225b. The solar wind velocity structure used in this study is shown in Figure 31.

B.2. Change of the Calculation of the Solar Wind Density as a Function of Heliolatitude

Unlike the solar wind speed, solar wind density outside the ecliptic plane is not easily available from measurements. Sokół et al. (2013) used a phenomenological relation between solar wind density and speed based on the density and speed data from three fast latitude scans of Ulysses and noticed that each Ulysses orbit required a different correlation formula. Since solar wind shows a clear secular evolution (McComas et al. 2013a), we felt it was no longer best to use the relations obtained from measurements completed during the previous solar cycle. Instead, to infer solar wind density as a function of heliolatitude for the current study, we use the relation of Le Chat et al. (2012)

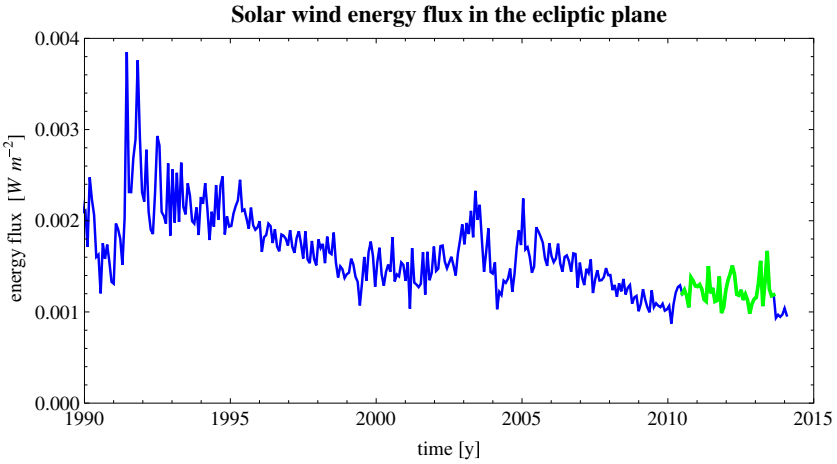

Figure 32. Energy flux of solar wind based on OMNI-2 Carrington rotation-averaged solar wind parameters, calculated from Equation (B1). The value adopted to compute the solar wind density as a function of heliolatitude from Equation (B2) is the average from the interval marked in green ($W = 0.00124$ W m^2).
(A color version of this figure is available in the online journal.)

based on Ulysses data that the solar wind energy flux

$$W = n_p(m_p + \xi_\alpha m_\alpha)\, v_{SW}\, (1/2 v_{SW}^2 + G\, M_{Sun}/R_{Sun}) \quad \text{(B1)}$$

varies very little with heliolatitude (is quasi-invariant) and thus could potentially be used to infer density if speed is known. Knowing the value of the solar wind energy flux in the ecliptic plane and the solar wind speed as a function of heliolatitude we can calculate the solar wind density at a given heliolatitude following the formula:

$$n_p(\phi) = 10^{-6} \frac{W}{v_p(\phi)\left(0.5 v_p^2(\phi) + C\right)(m_p + \xi_\alpha m_\alpha)} \quad \text{(B2)}$$

where m_p is a mass of the proton, m_α is mass of the alpha particle, ξ_α abundance of alpha particles in the solar wind, assumed to be 4% (e.g., Kasper et al. 2007), $v_p(\phi)$ solar wind speed as a function of heliolatitude ϕ, W solar wind energy flux, and $C = (M_{Sun} G/R_{Sun})$ (R_{Sun}: the radius of the Sun, M_{Sun}: the mass of the Sun, and G: gravity constant).

The total energy flux of solar wind is nearly constant after ~2008 ($W = 0.00124$ W m^2). In the present version of survival probability calculations, we switched from the previously used formula for solar wind density to the formula defined in Equation (B2) starting at the second half of 2012 (orbit 174a), when the solar maximum at the north hemisphere was observed. For the solar wind total energy flux value we adopted the mean obtained from averaging over the interval marked in Figure 32.

B.3. Modification of the Database with the In-Ecliptic Solar Wind

In 2013 February, OMNI2 released a new version of the in-ecliptic solar wind data, with various changes and modifications. The changes affect data since 1995. Their magnitude was only ~1% in the Carrington rotation-averaged solar wind speed, and up to about 10% in Carrington rotation-averaged solar wind number density, which resulted in such small changes in survival probabilities (much less than the overall uncertainty) that we decided to not recalculate the first five *IBEX* ENA maps.

B.4. Summary

In 2011, the 3D structure of the solar wind still generally resembled the structure typical for solar minimum conditions. Since that time, the Sun transitioned into the maximum activity phase, with a profound modification of the solar wind latitudinal structure. In this paper we take into account the evolution of the latitudinal structure of solar wind from ~2011.5 to ~2013.5. During this interval, the solar wind speed structure was characterized by a solar activity peak, with mixed speed solar wind in the northern hemisphere (see Figure 31). This means that the solar wind structure as a function of heliolatitude shows a distinct north–south asymmetry. This asymmetry was also indicated by, e.g., Chowdhury et al. (2013) based on a study of sunspot distribution. This asymmetry is clearly reflected in survival probabilities of H ENAs as illustrated in Figures 6 and 33. The north and south polar survival probabilities for two selected energies clearly show yearly modulations superimposed on a solar cycle trend related to the evolution of the latitudinal variation of the solar wind speed. The ecliptic probabilities, shown for the same energies for ram and anti-ram directions reflect their own yearly modulations, but the solar cycle-related trend is absent.

APPENDIX C

IBEX-HI DATA EFFICIENCY FACTOR OVER TIME

The *IBEX*-Hi ENA detection efficiency is tracked over time in a number of ways. First, the measurement of penetrating background from cosmic radiation (see Appendix A) does not show systematic variation over time as compared to ground-based cosmic-ray neutron monitors; this strongly implies that the efficiency of the channel electron multipliers (CEMs) at detecting secondary electrons is reasonably constant. Additionally, periodic gain tests of the CEMs are performed on orbit to determine if they are aging off of the "gain plateau," the range of operating voltage over which detection efficiency is nearly constant. Over the first five years, all three CEMs remain on the plateau and behave identically: there has been a shift of approximately 80 V on the location of the edge of the gain plateau relative to operating voltage, which has been held constant. Finally, the ratios of various coincidences during data collection allow the tracking of the absolute detection efficiency of each section of the *IBEX*-Hi detector (Funsten et al. 2005).

The process of determining the efficiency of the detector sections of *IBEX*-Hi is given in Appendix A of McComas et al. (2012b). Briefly, if the detection efficiency of sections A, B, and

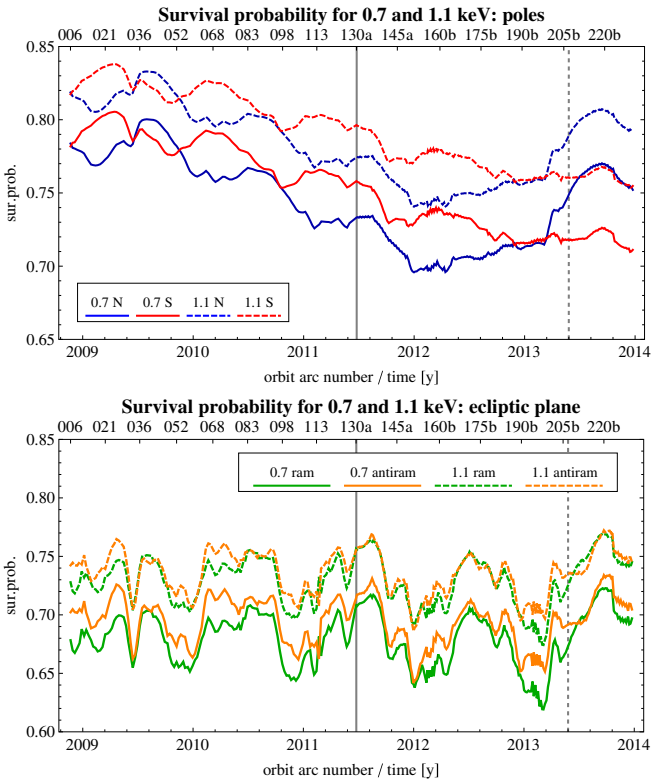

Figure 33. Survival probabilities for the north and south polar directions (upper panel) and for the in-ecliptic ram and anti-ram directions (lower panel), shown for the entire duration of the *IBEX* mission. The solid vertical line marks the beginning of Map 6; the dotted vertical line marks the freezing of the solar wind structure in the present calculation.

(A color version of this figure is available in the online journal.)

C of the *IBEX*-Hi detector are ε_A, ε_B, and ε_C respectively, then N incident ENAs will produce $N_{ABC} = N\,\varepsilon_A\,\varepsilon_B\,\varepsilon_C$ triple counts, qualified or unqualified, and $N_{BC} = N\,\varepsilon_B\,\varepsilon_C$ double counts in detector sections B and C. Thus, the efficiency of the first section of the detector is $\varepsilon_A = N_{ABC}/N_{BC}$; similar ratios supply ε_B and ε_C. The derived efficiency is for not only the CEM but the entire detector section, including, for instance, the secondary electron emission properties of the ultrathin carbon foils.

This derivation of efficiencies is exact in the absence of signals other than that produced by a spatially uniform hydrogen flux of time-independent energy spectrum entering *IBEX*-Hi. In practice, we limit data used to trend efficiency to the "good times" selected for heliospheric analysis in ESA settings 2–6 (see Appendix A), and subtract the penetrating background contribution to the doubles rates (N_{AB}, N_{AC}, and N_{BC}) and triples rate (N_{ABC}). The doubles rates are derived from the calculation of triples background rates from Appendix A and the doubles coincidence rates based on linearly interpolating and extrapolating the ratios of coincidence events observed in the background tests of orbits 13, 77, and 189. Imprecision in removal of these backgrounds limits the accuracy of the efficiency determination, and, in as much as the background ratios vary over time, the detection of any efficiency trends over time. In particular, the calculated drop in ε_A and ε_B over the year 2013 is almost certainly an artifact resulting from the doubles-to-triples background ratios dropping more slowly over time than is extrapolated from the 2009, 2010, and 2012 penetrating background tests, although confirmation awaits the results of the 2014 penetrating background test. Similarly, the initial drop in efficiencies mid-2009 appears only once the background ratios

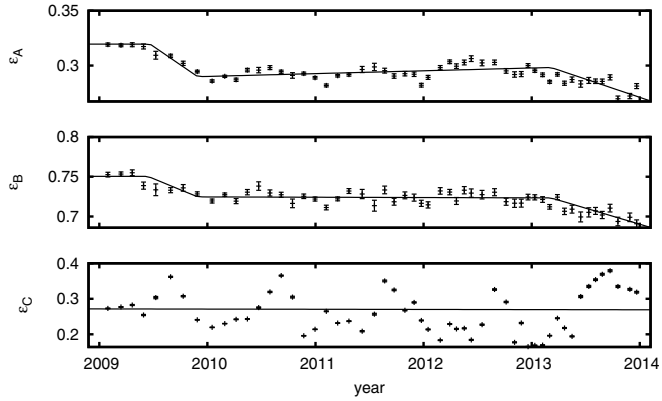

Figure 34. Detection efficiency of the three sections of the *IBEX*-Hi detector, as determined orbit by orbit from double and triple coincidence count ratios. Points are shown once every five orbit arcs. Error bars shown are predominantly from counting statistics.

are allowed to vary over time linearly between the 2009 and 2010 background test, and do not appear in McComas et al. (2012b), which used constant values consistent with the 2009 test.

A further complication arises because heavy species, such as oxygen, generate measurable AB coincidences but rarely generate triples, or any other coincidence involving CEM C, owing to their difficulty in penetrating even ultra-thin foils (e.g., McComas et al. 2004, and references therein) and the limited duration of the coincidence window Allegrini et al. 2008). The main source of excess AB coincidences is related to the "ion gun" background, discussed in Appendix D. In fact, the removal of the ion gun background requires as input an (estimated) efficiency of detector section C. The heavy-ion contamination in the AB counts severely limits the accuracy of ε_C determination, and consequently, coincidence-ratio determinations of detector-section efficiencies is really applicable only to ε_A and ε_B. Based on gain tests, it is reasonable to assume that CEMs B and C behave very similarly.

Figure 34 shows the efficiencies of the three detector sections calculated from coincidence ratios, averaged over five orbits or orbit arcs per point. For detector section C, no heavy ion contamination was removed: its presence is evident from the annual variation in ε_C well outside the statistical uncertainty shown, and the jump in calculated efficiency later in 2013, when the negative collimator voltage was increased. Detector sections A and B may have dropped slightly, but not beyond the bounds associated with linearly interpolating and extrapolating from the three background tests. Thus, for this study, efficiency of the *IBEX*-Hi detector as a whole has been taken to be constant over the first five years. Altogether, no change in efficiency is seen that would account for the general observed decrease in heliospheric ENA emissions.

APPENDIX D

REMOVAL OF THE "ION GUN" BACKGROUND IN *IBEX*-Hi DATA

We use the term "ion gun" to describe the background generated from ambient neutrals, such as desorbed or outgassing

atoms or molecules in the *IBEX*-Hi instrument, that become ionized within the positive collimator region of *IBEX*-Hi. From this location, they can be accelerated into the entrance conversion foil and masquerade as ENAs from outside the instrument (Wurz et al. 2009). Ionization is principally due to electrons in the local environment of the spacecraft that manage to get past the negative collimator and are then accelerated onto the positive collimator surfaces. UV light can also produce photoelectrons at the entrance surface of the charge conversion foils, where they are accelerated toward and into the collimator, which is biased at 7 kV. The negative collimator was designed to run at a voltage high enough to prevent electrons with <600 eV from reaching the positive collimator. However, very early in the mission it was observed that the negative collimator voltage potential also pulled solar wind ions around the sunshade and into the edge of the instrument, causing a different and larger background. Once this was established, collimator voltages were reduced, and from the start of science data collection onwards, the negative collimator voltage was set to reject electrons only below 80 eV. Testing in 2011 November to 2012 January determined that no statistically observable additional solar wind contamination could be correlated to an increase in negative collimator voltage which rejected electrons below 120 eV. Starting in 2013 April the negative collimator was increased accordingly, significantly reducing the ion gun signal.

The ion gun background shows up in triple coincidences almost entirely in *IBEX*-Hi energy pass bands 1, 2, 5, and 6 (see Funsten et al. 2009a, Table 6), and is negligible in ESAs 3 and 4. The signal in pass bands 1 and 2 arises from H_2O^+ produced in the positive collimator: the molecular ion dissociates on passing through the entrance foil, creating H^+ at 1/18 of the 7 kV potential between the positive collimator and the entrance foil (i.e., 389 eV) that is slightly reduced by energy lost in transiting the charge conversion foil. The signal in ESAs 5 and 6, which was not predicted in the background paper (Wurz et al. 2009), arrives at very close to half the collimator potential (i.e., 3.5 kV) and is therefore inferred to come from H_2^+ produced in the positive collimator. Additionally, the O^+ from H_2O^+ arrives over a broad range of straggled energies less than 16/18 of the 7 kV acceleration voltage. Its signal is limited almost entirely to coincidences of A and B. The observed ion gun signal that can be associated with hot electrons (e.g., by correlating with *WIND* 103 eV and 165 eV electron fluxes when *IBEX* is in the solar wind) is isotropic; the effect of photoelectrons was observed in orbit 114, when spacecraft pointing briefly allowed sunlight onto the collimator for a portion of the spin and produced a bright, anisotropic ion gun signal.

As a result of the oxygen signal in the AB coincidences, the amount of ion gun background in the qualified triples signal can be calculated using the rates of uniquely associated double and triple coincidence combinations, regardless of external information as to the hot electron flux. First, for energy pass bands 3 and 4, which do not see ion gun background in the qualified triples, the count rate is determined for AB coincidences in excess of what would be expected from the penetrating background rate (determined as in Appendix A and scaled to AB based on the on-orbit penetrating background test ratios) and from the ENA signal rate, using the penetrating-background-subtracted qualified ABC rate and an assumed efficiency for detector section C of $\varepsilon_C = 0.465 + (-0.015)$. This efficiency estimate comes from comparing the calibrated efficiencies of detector sections B and C to the on-orbit efficiency of detector section B. Then, over the intervals and observing angles considered to be good heliospheric viewing over the first four and a half years (before the negative collimator voltage was increased), slopes were determined between the minimum isotropic signal observed by *IBEX*-Hi in energy pass bands 1, 2, and 6, and the excess oxygen signal observed in energy pass bands 3 and 4. The minimum isotropic signal is defined as the minimum qualified triples count rate observed in the quietest contiguous 48 degree portion of spin, over a contiguous hour and a half of data collection, for intervals considered good for heliospheric data for energy pass bands 3 and 4. This correction assumes that all isotropic excess AB counts—that is to say, any heavy ion signal—is entirely due to ion-gun oxygen.

These slopes can then be applied to the good times of any specific orbit arc to correlate the qualified triple coincidence ion gun correction in energy pass bands 1, 2, and 6 from the calculated excess oxygen background. The correction is too small in energy range 5 for a statistically meaningful slope to be extracted by this technique, so for this range, the ESA 6 correction is scaled using the ion gun ratio during two intervals of very high ion gun background—an isotropic period from 2009 December, and the 2011 February orbit when *IBEX*'s pointing allowed sunlight to hit the collimator.

The minimum isotropic background signal in energy pass bands 1 and 2 correlates extremely well with the excess oxygen signal, which is to be expected since it all originates from the same H_2O^+ source. The signal in energy range 6, from H_2^+, also is highly correlated, though not as well as that in energy pass bands 1 and 2. No statistically significant time variation was observed in the correlation between the energy range 6 qualified ABC minimum isotropic background and the excess oxygen background of energy pass bands 3 and 4.

For intervals when *IBEX* is in the solar wind and *WIND* data is available, the excess oxygen background correlates well with 103 eV electron flux. Requiring the oxygen background to extrapolate to zero at zero electron flux provides values of ε_C consistent with the value used above, though with larger uncertainty values.

The triple coincidence ion gun count rate for a typical orbit was approximately 0.017 s^{-1} for energy range 6, 0.014 s^{-1} for energy range 2, and 0.01 s^{-1} for energy range 5, before the negative collimator voltage was increased. Energy range 1 is not currently used for heliospheric sky maps, but enabled quantification of this background early in the mission. In comparison, the penetrating background rate over the course of the first five years of data has ranged from about 0.06–0.03 s^{-1}. Ion gun corrections in the future should remain at least a factor of three smaller, owing to the recently increased negative collimator voltage.

APPENDIX E

SPUTTERING CORRECTIONS FOR *IBEX*-Lo H MAPS

This Appendix documents a new correction process for *IBEX*-Lo data that includes removing an apparent signal in an energy pass band caused by sputtering from higher energy neutrals. The first step in generating *IBEX*-Lo ~ 0.2 and ~0.4 keV maps is estimating differential ENA fluxes for H at these energies in the spacecraft frame. The differential fluxes simply represent the observed rates divided by observed energy times the geometric factor at the observed energy: $J_i = R_i/(E_i G_{ii})$, where J_i is an estimate of the differential energy flux at ESA step i with energy level E_i, the count rate is R_i, and G_{ii} is the geometric factor at this ESA step with units cm^2 sr keV keV^{-1}.

Table 5
H Sputtering Factors

Obs. Step i	Incident Flux step k	α_{ik}
5	6	0.29
5	7	0.068
5	8	0.016
5	9	0.016
6	7	0.52
6	8	0.061
6	9	0.015
7	8	0.75
7	9	0.061
8	9	0.75

The double index convention for the geometric factor G_{ik} considers the observed ESA step i and the incident flux that contributes from ESA step k where $k \geqslant i$. Therefore, for an incident flux J_k near the energy level E_k associated with ESA step k, the contribution to the observed rate R_i in ESA step i is $\Delta R_i = E_i\, G_{ik}\, J_k$.

The *IBEX*-Lo H maps show a feature in ESA steps 5 and 6 that are related to the interstellar flow observed in the *IBEX*-Lo O maps for the corresponding ESA steps. The interstellar neutral species O (and Ne) produce sputtered products, including H, C, and O at energies lower than that of the parent atom causing sputtering.

To determine the amount of sputtered H that needs to be subtracted from the maps, the composition of the interstellar flow in the two ESA steps 5 and 6 is needed. This information was derived from observed TOF spectra. The data was accumulated over one ISM flow season to acquire sufficient statistics. We analyzed ESA steps 5 and 6 separately because the ratio of the sputter product to the actual converted O is substantially different for these two energy pass bands. Because neutral H in the *IBEX*-Lo data is not only from sputtering, a contribution from the globally distributed ENA H source must be subtracted from the H peak in the TOF spectrum at a given ESA step. After subtraction of the globally distributed flux (Schwadron et al. 2011), we are able to determine the ratio of sputter H to O from the ISM.

In a given pixel of the H map, the O sputtering correction for the H differential flux $J^H{}_i$ is given by $J^H{}_i = J_i - J^O{}_i\, \chi_i$ where $J^O{}_i$ is the O differential energy flux in ESA step i and χ_i is the correction factor. Our analysis shows that $\chi_5 = 0.15 \pm 0.05$ and $\chi_6 = 0.01 \pm 0.008$.

The next step in solving for differential fluxes at incident particle energies is to correct for sputtering by H at energies above that in the observed ESA step. A bootstrap method was developed by Fuselier et al. (2012, 2014) that we adopt here. If we take $\alpha_{ik} = G_{ik}/G_{ii}$ (Table 5) then the estimated differential flux $J^H{}_i$ at ESA step i is a sum over the sputtering contributions from ESA step i and higher:

$$J_i^H = \Sigma_{j=i}^N \alpha_{ij} J_j \qquad \text{(E1)}$$

where $N = 9$ is the highest ESA step (*IBEX*-Hi flux at 2.73 keV) and we take $J^H{}_N = J_N$. Equation (E1) is inverted simply by iterative calculation of the differential flux J_i from ESA step i $N - 1$ down to step i, with the differential flux at each step given by

$$J_i = J_i^H - \Sigma_{j=i+1}^N \alpha_{ij} J_j. \qquad \text{(E2)}$$

We have used the fact that $\alpha_{ii} = 1$ by construction.

In producing the *IBEX*-Lo H maps, we have used the approximation that the geometric factor at each ESA step is constant throughout the mission. In the summer of 2012, the post-acceleration voltage was lowered from 16 to 7 keV, which reduced the time-of-flight efficiencies. However, almost simultaneously the transmission mode between *IBEX*-Lo and the data system was changed so that previously transmitted unused PHA events are now suppressed. This change has increased the throughput of the PHA events used for the ENA maps, thus roughly compensating for the efficiency reduction. While the team is currently working on accurately quantifying each of these factors, current estimates suggest that the net result of these geometric factor variations will lead to only minor changes to the maps well within statistical uncertainties.

REFERENCES

Allegrini, F., Bzowski, M., Dayeh, M. A., et al. 2012, ApJL, 749, L41
Allegrini, F., Crew, G. B., Demkee, D., et al. 2009, SSRv, 146, 105
Allegrini, F., Ebert, R. W., Alquiza, J., et al. 2008, RScI, 79, 096107
Bochsler, P., Kubiak, M. A., Möbius, E., et al. 2012, ApJS, 198, 13
Bzowski, M. 2008, A&A, 488, 1057
Bzowski, M., Kubiak, M. A., Möbius, E., et al. 2012a, ApJS, 198, 12
Bzowski, M., Sokół, J. M., Tokumaru, M., et al. 2013, Cross-Calibration of Past and Present Far UV Spectra of Solar System Objects and the Heliosphere (ISSI Scientific Report Series 13), ed. R. M. Bonnet, E. Quémerais, & M. Snow (New York: Springer), 67
Chalov, S. V., Alexashov, D. B., McComas, D., et al. 2010, ApJL, 716, L99
Chowdhury, P., Choudhary, D. P., & Gosain, S. 2013, ApJ, 768, 188
Dayeh, M. A., McComas, D. J., Allegrini, F., et al. 2012, ApJ, 749, 50
Frisch, P. C., Bzowski, M., Livadiotis, G., et al. 2013, Sci, 341, 1080
Funsten, H. O., Allegrini, F., Bochsler, P., et al. 2009a, SSRv, 146, 75
Funsten, H. O., Allegrini, F., Crew, G. B., et al. 2009b, Sci, 326, 964
Funsten, H. O., DeMajistre, R., Frisch, P. C., et al. 2013, ApJ, 776, 30
Funsten, H. O., Harper, R. W., & McComas, D. J. 2005, RScI, 76, 053301
Fuselier, S. A., Allegrini, F., Bzowski, M., et al. 2012, ApJ, 754, 14
Fuselier, S. A., Allegrini, F., Bzowski, M., et al. 2014, ApJ, 784, 89
Fuselier, S. A., Allegrini, F., Funsten, H. O., et al. 2009b, Sci, 326, 962
Fuselier, S. A., Bochsler, P., Chornay, D., et al. 2009a, SSRv, 146, 117
Fuselier, S. A., Funsten, H. O., Heirtzler, D., et al. 2010, GeoRL, 37, L13101
Heerikhuisen, J., Pogorelov, N. V., Zank, G. P., et al. 2010, ApJL, 708, L126
Kasper, J. C., Stevens, M. L., Lazarus, A. J., et al. 2007, ApJ, 660, 901
Kivelson, M. G., & Jia, X. 2013, JGR, 118, 6839
King, J. H., & Papitashvili, N. E. 2005, JGR, 110, A02104
Kucharek, H., Fuselier, S. A., Wurz, P., et al. 2013, ApJ, 776, 109
Le Chat, G., Issautier, K., & Meyer-Vernet, N. 2012, SoPh, 279, 197
Livadiotis, G., & McComas, D. J. 2009, JGR, 114, A11105
Livadiotis, G., & McComas, D. J. 2010, ApJ, 714, 971
Livadiotis, G., & McComas, D. J. 2013, SSRv, 175, 183
McComas, D. J., Alexashov, D., Bzowski, M., et al. 2012a, Sci, 336, 1291
McComas, D. J., Allegrini, F. A., Bochsler, P., et al. 2009a, SSRv, 146, 11
McComas, D. J., Allegrini, F., Bochsler, P., et al. 2009b, GeoRL, 36, L12104
McComas, D. J., Allegrini, F., Bochsler, P., et al. 2009c, Sci, 326, 959
McComas, D. J., Angold, N., Elliott, H. A., et al. 2013a, ApJ, 779, 2
McComas, D. J., Allegrini, F., Pollock, C. J., et al. 2004, RScI, 75, 4863
McComas, D. J., Bzowski, M., Frisch, P., et al. 2010, JGR, 115, A09113
McComas, D. J., Carrico, J. P., Hautamaki, B., et al. 2011a, SpWea, 9, S11002
McComas, D. J., Ebert, R. W., Elliott, H. A., et al. 2008, GeoRL, 35, L18103
McComas, D. J., Elliott, H. A., Goldstein, B. E., et al. 2003, GeoRL, 30, 1517
McComas, D. J., Funsten, H. O., Fuselier, S. A., et al. 2011b, GeoRL, 38, L18101
McComas, D. J., Dayeh, M. A., Allegrini, F., et al. 2012b, ApJS, 203, 1
McComas, D. J., Dayeh, M. A., Funsten, H. O., et al. 2013b, ApJ, 771, 77
McComas, D. J., Lewis, W. S., & Schwadron, N. A. 2014, Rev. Geophys., 52, 118
Möbius, E., Bochsler, P., Bzowski, M., et al. 2009, Sci, 326, 969
Möbius, E., Bochsler, P., Bzowski, M., et al. 2012, ApJS, 198, 11
Möbius, E., Liu, K., Funsten, H., Gary, S. P., & Winske, D. 2013, ApJ, 766, 129
National Research Council (NRC) 2013, Solar and Space Physics: A Science for a Technological Society (Washington, DC: The National Academies Press)
Opher, M., Alouani Bibi, F., Toth, G., et al. 2009, Natur, 462, 1036
Petrinec, S. M., Dayeh, M. A., Funsten, H. O., et al. 2011, JGR, 116, A07203
Reisenfeld, D. B., Allegrini, F., Bzowski, M., et al. 2012, ApJ, 747, 110

Rodriguez, Moreno, D. F., Wurz, P., Saul, L., et al. 2013, A&A, 557, A125
Scherrer, J., Carrico, J., Crock, J., et al. 2009, SSRv, 146, 35
Schwadron, N. A., Adams, F. C., Christian, E. R., et al. 2014, Sci, 343, 988
Schwadron, N. A., Allegrini, F., Bzowski, M., et al. 2011, ApJ, 731, 56
Schwadron, N. A., Bzowski, M., Crew, G. B., et al. 2009, Sci, 326, 966
Schwadron, N. A., & McComas, D. J. 2013, ApJ, 764, 92
Siewert, M., Fahr, H.-J., & McComas, D.J. 2013, A&A, 551, A58
Sokół, J. M., Bzowski, M., Tokumaru, M., et al. 2013, SoPh, 285, 167
Tokumaru, M., Kojima, M., & Fujiki, K. 2012, JGR, 117, A06108
Witte, M. 2004, A&A, 426, 835
Wurz, P., Fuselier, S. A., Möbius, E., et al. 2009, SSRv, 146, 173
Zank, G. P., Heerikhuisen, J., Wood, B. E., et al. 2013, ApJ, 763, 20